Geophysical Journal International

Geophys. J. Int. (2014) **197,** 396–413
Advance Access publication 2014 January 24

doi: 10.1093/gji/ggt511

Mantle transition zone structure beneath India and Western China from migration of *PP* and *SS* precursors

Stephan Lessing,[1] Christine Thomas,[1] Sebastian Rost,[2] Laura Cobden[1,3] and David P. Dobson[4]

[1] *Institute of Geophysics, Westfälische Wilhelms-Universität Münster, Corrensstraße 24, D-48149 Münster, Germany. E-mail: stephan.lessing@uni-muenster.de*
[2] *School of Earth and Environment, Institute of Geophysics and Tectonics, University of Leeds, Leeds LS2 9JT, United Kingdom*
[3] *Department of Earth Sciences, Utrecht University, Budapestlaan 4, NL-3584CD Utrecht, the Netherlands*
[4] *Department of Earth Sciences, University College London, Gower Street, London WC1E 6BT, United Kingdom*

Accepted 2013 December 17. Received 2013 November 5; in original form 2013 September 9

SUMMARY

We investigate the seismic structure of the upper-mantle and mantle transition zone beneath India and Western China using *PP* and *SS* underside reflections off seismic discontinuities, which arrive as precursors to the *PP* and *SS* arrival. We use high-resolution array seismic techniques to identify precursory energy and to map lateral variations of discontinuity depths. We find deep reflections off the 410 km discontinuity ($P^{410}P$ and $S^{410}S$) beneath Tibet, Western China and India at depths of 410–440 km and elevated underside reflections of the 410 km discontinuity at 370–390 km depth beneath the Tien Shan region and Eastern Himalayas. These reflections likely correspond to the olivine to wadsleyite phase transition. The 410 km discontinuity appears to deepen in Central and Northern Tibet. We also find reflections off the 660 km discontinuity beneath Northern China at depths between 660 and 700 km ($P^{660}P$ and $S^{660}S$) which could be attributed to the mineral transformation of ringwoodite to magnesiowuestite and perovskite. These observations could be consistent with the presence of cold material in the middle and lower part of the mantle transition zone in this region. We also find a deeper reflector between 700 and 740 km depth beneath Tibet which cannot be explained by a depressed 660 km discontinuity. This structure could, however, be explained by the segregation of oceanic crust and the formation of a neutrally buoyant garnet-rich layer beneath the mantle transition zone, due to subduction of oceanic crust of the Tethys Ocean. For several combinations of sources and receivers we do not detect arrivals of $P^{660}P$ and $S^{660}S$ although similar combinations of sources and receivers give well-developed $P^{660}P$ and $S^{660}S$ arrivals. Our thermodynamic modelling of seismic structure for a range of compositions and mantle geotherms shows that non-observations of $P^{660}P$ and $S^{660}S$ arrivals could be caused by the dependence of underside reflection coefficients on the incidence angle of the incoming seismic waves. Apart from reflections off the 410 and 660 km discontinuities, we observe intermittent reflectors at 300 and 520 km depth. The discontinuity structure of the study region likely reflects lateral thermal and chemical variations in the upper-mantle and mantle transition zone connected to past and present subduction and mantle convection processes.

Key words: Phase transitions; Body waves; Wave scattering and diffraction; Asia.

1 INTRODUCTION

Convection in Earth's mantle transports heat from the core–mantle boundary to the Earth's surface. Hot mantle material rises from the lower mantle towards the surface while cold crustal and lithospheric material from the surface are brought into the mantle at subduction zones. These convection movements, if mapped properly, can give important insights into the structure, evolution, and dynamics of our planet. The effect of warm upwellings and cool downwellings on the global seismic structure of the mantle has been inferred from global seismic tomography (e.g. Grand *et al*. 1997; Megnin & Romanowicz 2000; Li *et al.* 2008; Ritsema *et al.* 2011), with reduced seismic wave velocities frequently interpreted as representing hotter mantle regions (upwellings, plumes), and increased seismic wave velocities often interpreted as corresponding to cooler mantle regions (subduction zones). However, wave velocities may also be strongly influenced by changes in chemistry (e.g. Trampert *et al.* 2004).

An alternative way to constrain the structure of the mantle is the deflection of seismic discontinuities within the mantle (e.g. Shearer 2000). The two major seismic discontinuities bounding the mantle transition zone between the upper and lower mantle are found at approximately 410 and 660 km depth (e.g. Grand & Helmberger 1984; Revenaugh & Jordan 1991; Shearer & Masters 1992; Flanagan & Shearer 1998, 1999; Gu *et al.* 1998; Schmerr & Garnero 2006; Deuss 2009). Recent estimates of the globally averaged depth of the 410 and 660 km discontinuity by Houser *et al.* (2008) give average depths of 410 and 650 km. Despite variations in depth of the discontinuities we will refer to them as the 410 and 660 km discontinuities. These discontinuities are likely due to the solid-solid phase transition of olivine to wadsleyite near 410 km depth and the dissociation reaction of ringwoodite to magnesiowuestite and perovskite near 660 km depth (e.g. Ringwood 1969) within the olivine component of the mantle material. The depths of these discontinuities are sensitive to the ambient temperature and composition and can therefore be used to map the up- and downwellings of the mantle convection (e.g. Bina & Helffrich 1994; Helffrich 2000; Weidner & Wang 2000). The pressure–temperature dependence of a phase transition or mineral reaction is quantified by its Clapeyron slope. Recent measurements give a Clapeyron slope of +4.0 MPa K^{-1} for the olivine to wadsleyite phase transition (Katsura *et al.* 2004) and a negative Clapeyron slope of –1 to –3 MPa K^{-1} for the dissociation of ringwoodite to magnesiowuestite and perovskite (Irifune *et al.* 1998; Shim *et al.* 2001; Fei *et al.* 2004). As the Clapeyron slopes for these two reactions have opposite signs, the depths of the reactions should be anticorrelated for thermal anomalies (Helffrich 2000), leading to a thinned mantle transition zone in warm and a thickened transition zone in cold regions. In several regions an anticorrelation of discontinuity depths has been observed (e.g. Gu *et al.* 1998). Nonetheless, several observations also indicate that the depths of the 410 and 660 km discontinuities can be correlated in some regions (e.g. Gossler & Kind 1996, Schmerr & Garnero 2006).

Despite olivine being the dominant mineral phase of the mantle, the minerals of the pyroxene–garnet system will lead to more complicated phase relationships. Mineral transformations in the pyroxene–garnet component of the mantle and the interaction of the pyroxene–garnet system with the olivine system might lead to the observed behaviour of the mantle transition zone discontinuities that is not purely thermal in origin (e.g. Vacher *et al.* 1998; Weidner & Wang 1998, 2000). In cold regions of the mantle, for example, influenced by subduction, mineral physical experiments indicate two additional solid–solid phase transitions: the exothermic garnet to ilmenite phase transition (Wang *et al.* 2004) and endothermic ilmenite to perovskite phase transition (Wang *et al.* 2004). The completion of the garnet to perovskite phase transition near 720 km depth can give rise to an additional change in seismic wave velocities and densities below 660 km depth (Stixrude 1997; Weidner & Wang 1998). In hot regions, the dissociation of ringwoodite to magnesiowuestite and perovskite is replaced by the exothermic garnet to perovskite phase transition (Hirose 2002) due to the instability of ringwoodite at high temperatures (Gasparik 1996a,b; Weidner & Wang 1998; Irifune *et al.* 1998). Therefore, the observation of the fine scale structure of the multiple discontinuities of the transition zone will allow the analysis of both thermal and chemical heterogeneities in tectonically active regions such as subduction zones (e.g. Simmons & Gurrola 2000; Deuss *et al.* 2006; Thomas & Billen 2009).

In this study, we investigate the fine scale structure of the multiple seismic discontinuities of the upper-mantle and mantle transition zone beneath India and Western China. The mantle transition zone

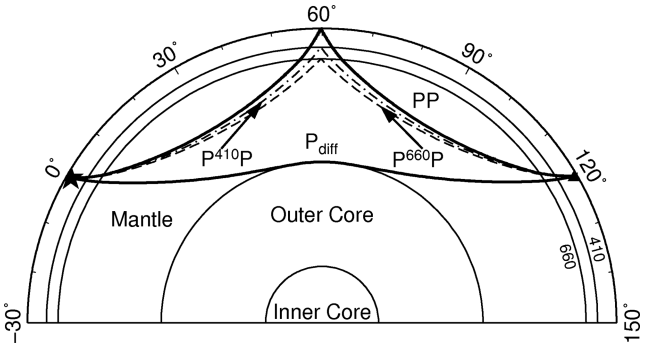

Figure 1. Example ray paths of *PP*, $P^{410}P$ and P_{diff}. Underside reflections occur at the midpoint of the seismic ray path. The ray paths of *SS* and its precursors are similar.

beneath the Indian–Eurasian collision zone is influenced by a long-term subduction history starting 150 Ma which includes collisions of volcanic arcs of the Tethys Ocean, and finally of the Indian Plate, with the Eurasian Plate (Molnar & Tapponnier 1975; Yin & Harrison 2000; Haines *et al.* 2003; Tapponnier *et al.* 2001). During this time oceanic crust and lithospheric mantle were subducted into the mantle. The seismic structure of the mantle beneath the Indian–Eurasian collision zone has been investigated previously with surface waves (Brandon & Romanowicz 1986; Curtis & Woodhouse 1997; Lebedev & van der Hilst 2008), seismic tomography (van der Voo *et al.* 1999; Tilmann *et al.* 2003; Li *et al.* 2008) and receiver functions (e.g. Kosarev *et al.* 1999; Kind *et al.* 2002).

For our investigation of upper-mantle and mantle transition zone structure we use *PP* and *SS* precursors which represent underside reflections off seismic discontinuities (Fig. 1) halfway between the source and receiver (King *et al.* 1975; Shearer 1991). Underside reflections of *PP* or *SS* off a reflector are denoted as P^dP or S^dS, with *d* indicating the depth of the reflecting discontinuity. Due to the reflection coefficients at the discontinuities the underside reflections are rarely visible on individual seismograms. Previously, large numbers of globally recorded long-period or broad-band seismograms which sample a certain region have been stacked to enhance the signal-to-noise ratio (SNR) of the precursor signals (e.g. Shearer 1991; Gu *et al.* 1998; Schmerr & Garnero 2006; Deuss 2009). These stacks have robustly detected $P^{410}P$, $S^{410}S$ and $S^{660}S$ arrivals (e.g. Flanagan & Shearer 1998, 1999). However, arrivals of $P^{660}P$ are not detected in most studies (Shearer 1991; Estabrook & Kind 1996; Rost & Weber 2002; Deuss 2009). A few studies have detected intermittent reflectors off 660 km depth using *PP* underside reflections (Deuss *et al.* 2006; Thomas & Billen 2009; Schmerr & Thomas 2011), leading to the conclusion that the *P*-wave velocity contrast may be about 50 per cent smaller (Estabrook & Kind 1996; Flanagan & Shearer 1998) than given by the 1-D seismic reference models PREM (Dziewonski & Anderson 1981) or IASP91 (Kennett & Engdahl 1991) or that the 660 km discontinuity might be a gradient rather than a first-order discontinuity (Rost & Weber 2002). Deuss *et al.* (2006) and Thomas & Billen (2009) also observe multiple discontinuities near 660 km depth and frequency-dependent behaviour of the seismic signals, which may be related to short-scale lateral variations of the aluminum content. Due to the stacking of *PP* waveforms, signals from variable depths might interfere destructively and might not be observable in the stacked waveforms.

Non-observations of the $P^{660}P$ reflections are difficult to reconcile with the results of mineral physical experiments. High pressure-high temperature experiments indicate that the dissociation reaction

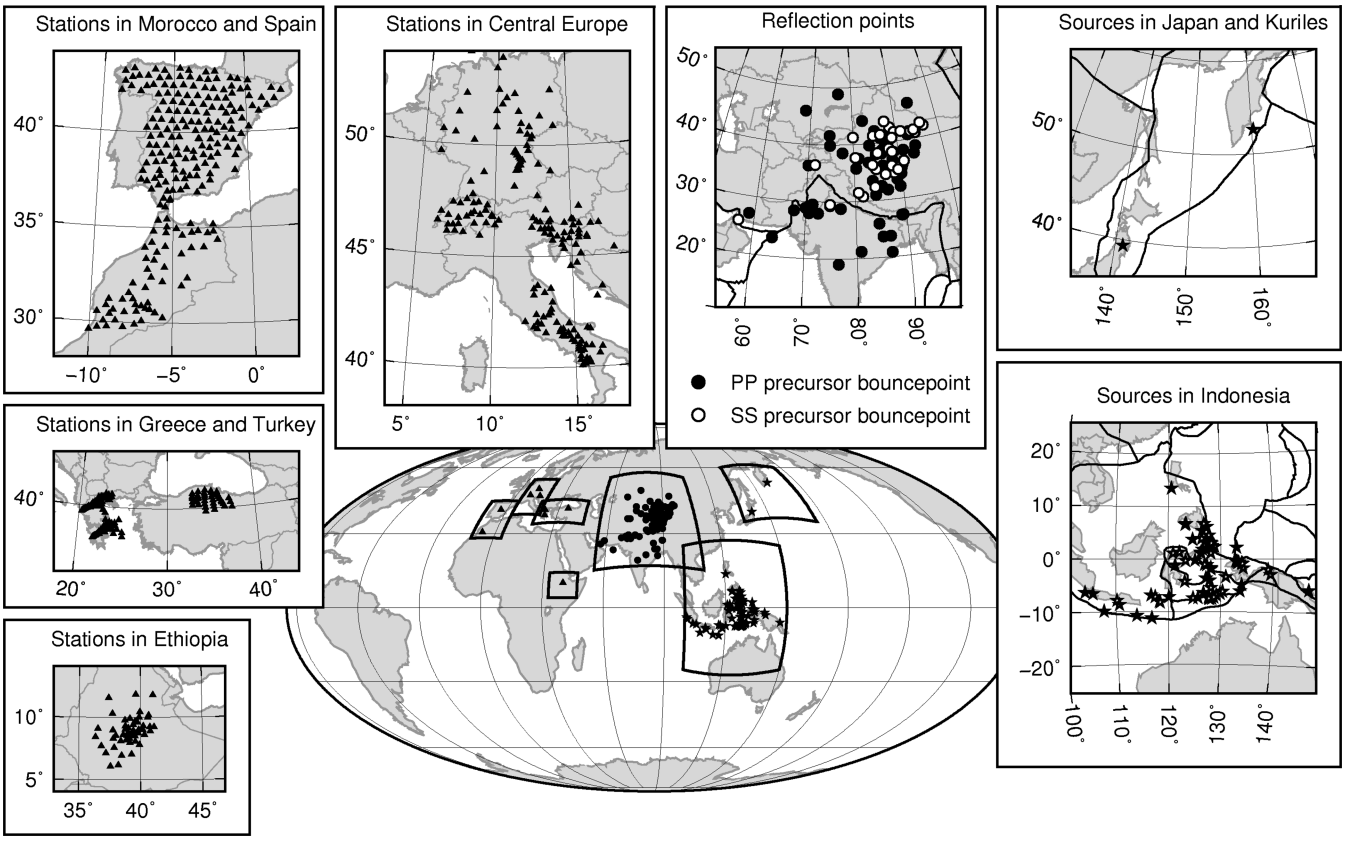

Figure 2. Maps of the seismic sources and receivers used in this study. Triangles show locations of central stations for each array used. Stars indicate event locations and circles denote reflection points of *PP* and *SS* at the surface. Japan and Kuriles subduction zone source region with events used in this study (stars). Sumatran subduction zone source region with events used in this study (stars). Location of *PP* and *SS* surface reflection points. Plate boundaries are from Bird (2003).

of ringwoodite to magnesiowuestite and perovskite occurs within a narrow pressure interval of 0.1–0.5 GPa (i.e. ∼2–10 km) for a range of temperatures (e.g. Litasov *et al.* 2005a), and thermodynamic modelling gives *P*-wave impedance increases (i.e. the product of density and *P*-wave velocity) of 6–8 per cent for pyrolite mantle compositions (e.g. Vacher *et al.* 1998). We would therefore expect that short-period *P*-wave energy is effectively reflected by such a sharp transition (e.g. Deuss 2009; Thomas & Billen 2009). Interestingly, receiver function analysis frequently shows the discontinuity (e.g. Vinnik 1977; Dueker & Sheehan 1997; Kosarev *et al.* 1999; Simmons & Gurrola 2000; Kind *et al.* 2002; Andrews & Deuss 2008) and there is evidence for a sharp 660 km discontinuity from observations of PKIKPPKIKP (or denoted as $PKPPKP_{df}$ or $P'P'_{df}$) underside reflections in several regions (Nakanishi 1986, 1988; Benz & Vidale 1993; Xu *et al.* 1998; Day & Deuss 2013).

In our study, we take advantage of the dense seismic networks of permanent and temporary broad-band stations across Europe, as well as several temporary seismic networks in Morocco, Spain, Greece, Turkey, Israel and East Africa. We use array seismic processing methods (Rost & Thomas 2002; Rost & Thomas 2009), for example, vespagrams and a migration technique, to detect *PP* and *SS* underside reflections off upper-mantle and mantle transition zone discontinuities. We aim to interpret our observations of underside reflections semi-quantitatively in terms of thermal and chemical heterogeneities in the upper-mantle and mantle transition zone, on the basis of experimental mineral physical data and thermodynamic modelling.

2 DATA SELECTION

The data set consists of broad-band velocity seismograms for several source–receiver combinations whose *PP* and *SS* surface reflection points sample the upper-mantle and mantle transition zone in our study area (Fig. 2 and Tables S1). Earthquake sources are located in the subduction zones south of Sumatra and Java, in the Banda arc and Molucca Sea in Indonesia, as well as in the subduction zones of the Philippines and Japan. For our source–receiver combinations, *PP* and *SS* waves propagate mainly in SE–NW direction. Nonetheless, using paths from Japan to Ethiopia (i.e. NE–SW across the study area) allows us to study the region with crossing paths.

We investigate *PP* arrivals on the vertical component whereas *SS* arrivals are analysed on the transverse component after rotation of the horizontal components to the great circle arc. We use earthquakes with magnitudes $5.8 \leq M_W \leq 7.5$ to ensure sufficient precursor energy before the *PP* and *SS* arrivals and simple source time functions. We measure the SNR of unfiltered traces as the ratio of the peak-to-peak amplitude in a 50 s time window around the *PP*/*SS* arrival predicted by ak135 (Kennett *et al.* 1995) and the peak-to-peak amplitude of a 50 s time window before the predicted P/P_{diff} or S/S_{diff} arrival. Only unfiltered data with SNR > 2, with at least 12 traces per event and visible and impulsive *PP*/*SS* wavelets are kept for further analysis. The traces are aligned on the *PP* or *SS* arrival times predicted by ak135 (Kennett *et al.* 1995), and the alignment is further optimised using adaptive stacking (Rawlinson & Kennett 2004). Adaptive stacking corrects for mislocation effects

due to varying station elevations and the seismic structure beneath the stations (Krüger & Weber 1992; Jacobeit *et al.* 2013).

3 DATA PROCESSING

We analyse the data set using four array processing methods: vespagrams, sliding-window frequency–wavenumber analysis, slowness–backazimuth analysis and a migration technique (Rost & Thomas 2002). For the source–receiver distribution of each event, we calculate synthetic seismograms using the reflectivity method (Fuchs & Müller 1971; Müller 1985) using the 1-D velocity model ak135 (Kennett *et al.* 1995), density by Montagner & Kennett (1995) and attenuation of PREM (Dziewonski & Anderson 1981), and process synthetic data in the same way as the broad-band data, to ensure the accuracy of our data processing.

We calculate 4th root vespagrams (Davies *et al*. 1971; Muirhead & Datt 1976) for the theoretical backazimuth of the station closest to the geometrical centre of the used array (Fig. 3b). This allows us to detect *PP* and *SS* underside reflections by matching the observed traveltimes and slowness values of seismic arrivals with traveltimes and slowness values for this distance as predicted by ak135 (Kennett *et al.* 1995). Each broad-band seismogram section is filtered with second-order butterworth bandpass filters and corner periods between 2 and 20 s, 3 and 10 s, 5 and 25 s, 6 and 50 s, 8 and 75 s, 15 and 75 s and 10 and 100 s. We use a range of filters in order to investigate frequency-dependent behaviour of the observed signals. Arrivals with slowness values similar to *PP* and *SS* are only considered for further analysis if they are clearly separated from arrivals of depth phases (i.e. pPP, $pP^{410}P$, $pP_{\rm diff}$, etc.), top-side reflections (i.e. $P_{410}pP_{\rm diff}$ or $P_{660}pP_{\rm diff}$ on the source side, $Pp_{410}p$ or $Pp_{660}p$ on the receiver side), converted phases (e.g. $S_{410}pP_{\rm diff}$ or $S_{660}pP_{\rm diff}$ on the source side, $Sp_{410}p$ or $Sp_{660}p$ on the receiver side) and PKP arrivals.

We also study the data using the sliding-window frequency–wavenumber analysis (Capon 1973; Rost & Weber 2002) for arrays with apertures less than 2° and slowness–backazimuth analysis (King *et al.* 1976) for arrays with apertures larger than 2° (Fig. 3c). Both methods simultaneously measure the slowness and backazimuth of an incoming wave front within a specified time window, and help to distinguish seismic wave energy propagating along the great circle path from seismic wave energy scattered or reflected off the great circle path. We only consider arrivals (i) with slowness values within ±0.5 s deg^{-1} of the predicted *PP* and *SS* precursor slowness values and (ii) with maximum backazimuth deviations of ±5° from the theoretical backazimuth of the great circle arc to avoid the analysis of off-azimuth scattered energy also arriving as *PP* precursors (Rost *et al.* 2008).

We determine the depth of the discontinuities using a migration technique (Thomas & Billen 2009; Schmerr & Thomas 2011). The migration backprojects *PP* and *SS* precursory energy to its reflection point and reduces the size of the Fresnel zone, thus improving the horizontal resolution of the observations (Rost & Thomas 2009). A three dimensional grid is placed around the theoretical *PP* or *SS* reflection point covering an area of 40° × 40° with 1° gridpoint spacing. The depth of the grid ranges from 0 to 900 km with 5 km depth increments. For each event, ray tracing through ak135 (Kennett *et al.* 1995) is used to calculate traveltimes from the source location to each gridpoint and from each gridpoint to each receiver. The traveltimes to each depth layer are corrected for variations in crustal thickness and lateral mantle heterogeneity. We use 1-D ray tracing through the global crustal model CRUST2.0 (Bassin *et al.* 2000), the *P*-wave tomography model MITP08 (Li *et al.* 2008) for *PP*, and the *S*-wave tomography model S40RTS (Ritsema *et al.* 2011) for *SS* waves and compute traveltime corrections for the entire path of *PP* and *SS* and their precursory arrivals (Schmerr & Garnero 2006). Using the traveltimes and traveltime corrections for each gridpoint, the individual seismograms are shifted and stacked. We apply linear and 4th root stacking methods (Davies *et al*. 1971; Muirhead & Datt 1976), and measure the amplitude of the stacked traces from each gridpoint within a 3 s time window around the theoretical arrival time of the precursor. Subsequently the stacked amplitude is assigned to the gridpoint. Regions of enlarged amplitude indicate possible origins of underside reflections. The resulting migrated energy recreates the saddle-shaped form of the *PP* and *SS* Fresnel zone due to the minimum–maximum traveltime of underside reflected waves (Fig. 4) (Choy & Richards 1975; Thomas & Billen 2009; Rost & Thomas 2009).

We try to estimate the statistical robustness of our observations, for example, with bootstrap resampling (Efron & Tibshirani 1986), a technique routinely applied in global studies of *PP* and *SS* precursors (e.g. Deuss *et al.* 2006; Schmerr & Garnero 2006). The major part of our array recordings in this particular study, however, come from small arrays and usually contain less than 20 seismograms per event. Proper bootstrapping requires 50–200 random samples for estimating the confidence intervals (Efron & Tibshirani 1986). We calculate a simplified bootstrapping in the vespagrams for our events in which we randomly replace two seismic traces by copies of two remaining seismograms. We detect the arrivals of the underside reflections in all 'bootstraps', and we are confident that our observations are robust.

The migration technique illuminates potential places of reflections of *PP* or *SS* and their precursors (Thomas & Billen 2009). However, reverberations of the non-*PP* or non-*SS* and related phases may also map into the 3-D grid with significant energy away from the theoretical reflection point, especially if the seismograms have been filtered with long-period bandpass filters before migration. Comparisons of migration results with vespagrams and slowness–backazimuth measurements help to discriminate *PP* and *SS* precursor energy from other seismic arrivals. We discard arrivals which are not clearly separated from the non-precursory energy. We determine the depth of the discontinuities from amplitude–depth profiles (Thomas & Billen 2009) which show the amplitude in each depth layer of the grid at the theoretical reflection point between the source location and the reference station of the array.

We estimate the systematic error in discontinuity depth by our summing traveltime corrections for crustal thickness and mantle heterogeneity at 410 and 660 km depth and by converting the residual times into depth perturbations using ak135 (Kennett *et al.* 1995). The traveltime corrections for crustal and mantle heterogeneity result in depth variations of ±8 km. For the vertical resolution of the migration scheme we calculate synthetic reflectivity seismograms for a range of dominant periods for velocity models based on ak135 (Kennett *et al.* 1995), including two separate reflectors at 410 km depth which have the half of the density, *P* and *S* wave contrast and a given spacing between each other. We find that two neighbouring reflectors with a vertical spacing of 30 km or larger are well resolved. For the lateral uncertainties of our observations, we use an ellipse at the centre of the first 1-D Fresnel zone, following Rost & Weber (2002) and Thomas & Billen (2009). With this criterion, the Fresnel zone is approximately 4° × 8° (±400 × 800 km at 410 km depth) around the ray theoretical point of reflection for a 5 s *PP* wave.

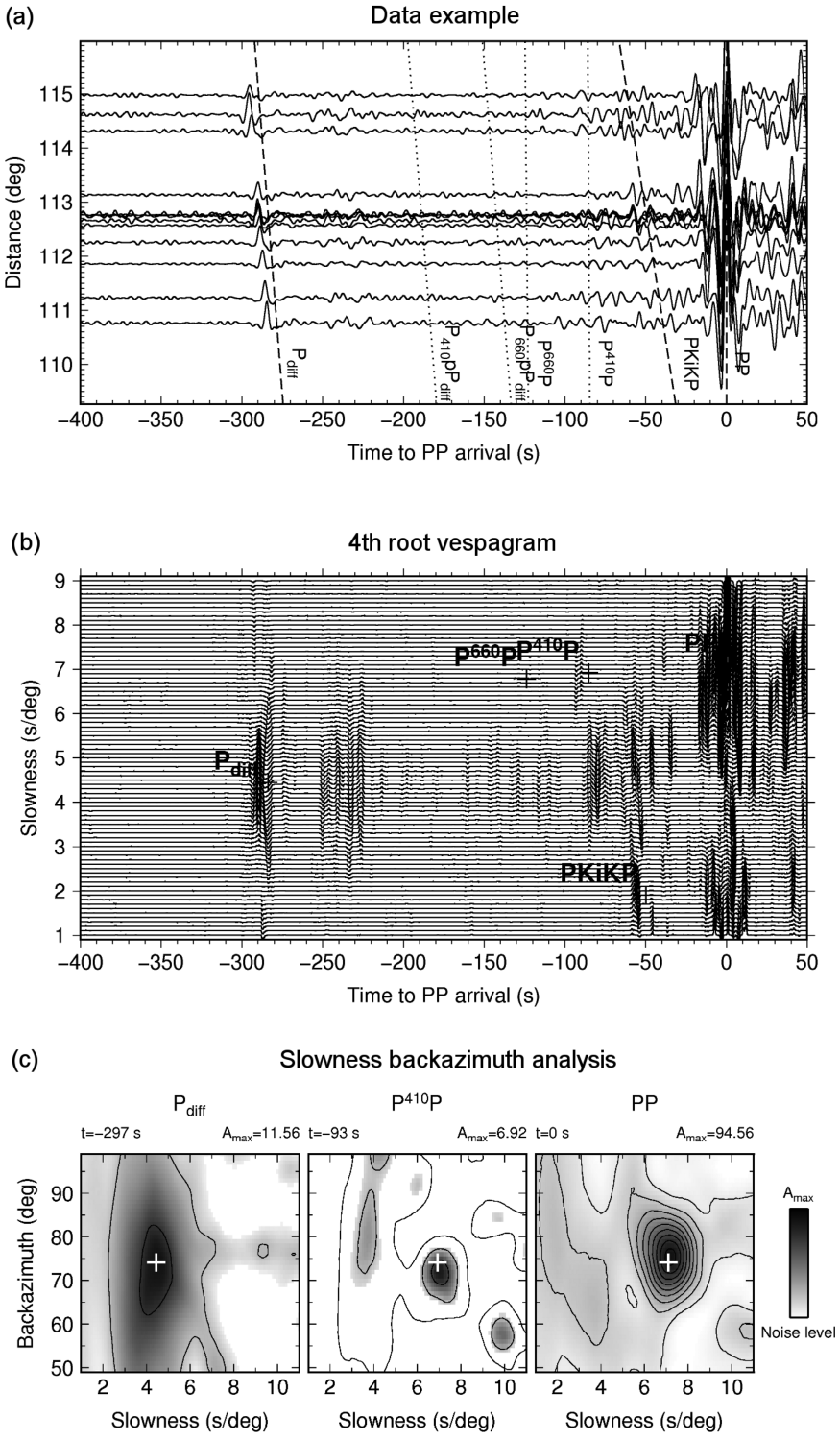

Figure 3. Waveforms, vespagram and slowness–backazimuth analysis of the earthquake occurring on 1994 July 13 for a detection of $P^{410}P$ and a non-detection of $P^{660}P$. (a) Seismograms were recorded at stations of the German Regional Seismic Network (GRSN), aligned on the maximum amplitude of *PP* and filtered with a second order butterworth bandpass and corner frequencies of 10 and 100 s. The maximum of the *PP* waveform is normalized. The dashed lines show arrival of major seismic phases, the dotted lines show arrival of minor phases which are reflections or conversions of major phases at seismic discontinuities (e.g. Pp_{410}p and Pp_{660}p). (b) Fourth root vespagram of the event shown in (a). The crosses mark the theoretical traveltimes and slowness values of the labelled phases assuming the ak135 velocity model. The traveltimes and slowness values of both figures are calculated with the TauP toolkit (Crotwell *et al.* 1999). (c) Slowness–backazimuth analysis for the P_{diff}, $P^{410}P$ and *PP* arrivals. Times are given relative to the *PP* arrival. The time windows are 10 s wide, the time step between slowness–backazimuth measurements is 1 s. The theoretical slowness and backazimuth of each seismic phase is marked with a white cross; slowness values are calculated for the reference station assuming ak135 seismic structure (Kennett *et al.* 1995).

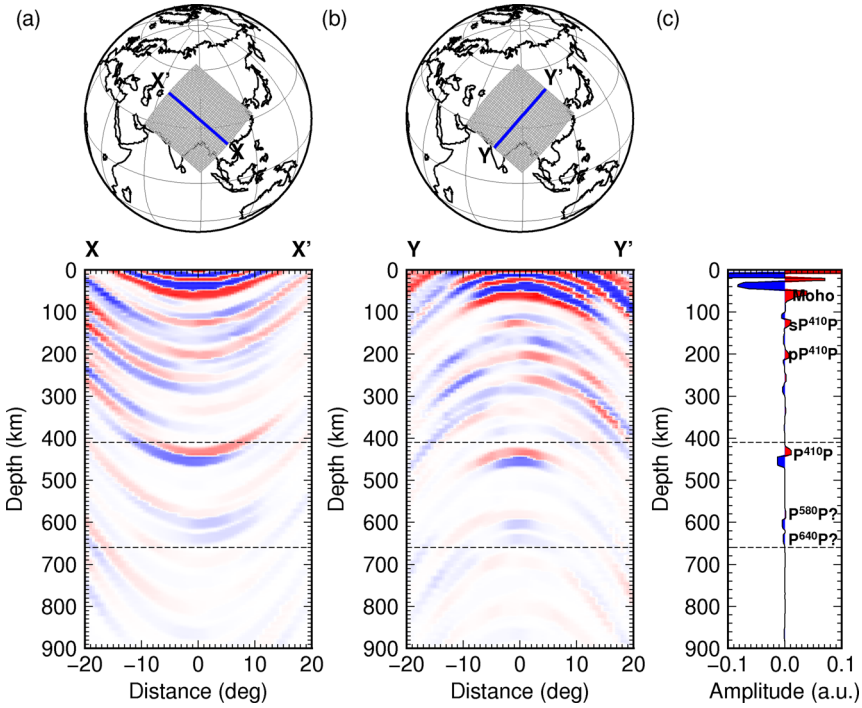

Figure 4. Migration results of the 1994 July 13 earthquake shown in Fig. 3. (a) Cross-section through the migrated data along the great circle path indicated by the points X and X′ on the globe above. Positive amplitudes are in red, negative amplitudes are in blue. (b) Cross-section through the migrated data perpendicular to the great circle path indicated by the points Y and Y′ on the globe above. Due to saddle shaped Fresnel zone for *PP*, *PP* underside reflections along the great circle path are curved downwards, while being curved upwards perpendicular to the great circle path. The details are the same as in part (a). (c) Amplitude–depth profile at the theoretical reflection point.

4 RESULTS

We compare the results of vespagrams, slowness–backazimuth analyses, sliding window fk-analyses and migration images to measure the depth at which *PP* and *SS* precursory arrivals reflect off upper-mantle and mantle transition zone discontinuities (Figs 3 and 4). The *PP* precursors arrive in a slowness range of 6.5–7.8 s deg^{-1} at the arrays depending on the epicentral distance. The arrivals of the observed *SS* precursors have slowness values ranging from 12.4 to 14.0 s deg^{-1}. Nonetheless, due to the limited aperture of the arrays and their therefore limited resolution in wavenumber space, the slowness resolution of the arrivals depends on the aperture of the array and the data frequency band (Fig. 3b).

We analyse the events with a range of bandpass filters to investigate the frequency dependent behaviour of the underside reflections. The majority of the events for *PP* precursors show clear arrivals of the *PP* surface reflection in unfiltered data. We observe robust *PP* underside reflections in the longer period range from 6 to 50 s and for longer periods in our vespagrams and migrations. Most reflections at ∼660 km depth are discernible in vespagrams and migration results when the seismograms are filtered between 10 and 100 s. In our data set, we rarely observe clear *SS* waveforms in unfiltered data. Most events with impulsive *SS* waveforms which match our SNR criterion are filtered with bandpasses between 15 and 75 s. Our analysis indicates that the variations of depth estimates due to the frequency dependence are small and within the uncertainties of our measurements.

We want to include the reflector thickness as an additional constraint for our interpretation. We test whether we could infer the thickness of a reflector from the frequency dependent behaviour of amplitudes directly from our observed *PP* precursor waveforms. We use ak135-f (Kennett *et al.* 1995; Montagner & Kennett 1995) and attenuation of PREM (Dziewonski & Anderson 1981) as a reference model and change the discontinuous contrasts of seismic properties into a set of gradients around 410 km depth, including linear gradients, sigmoidal gradients as proposed by Helffrich & Bina (1994) and Stixrude (1997) for divariant phase transitions (i.e. for phase transitions like Fe-bearing olivine to Fe-bearing wadsleyite), and parabolic gradients similar to Weidner & Wang (2000). The gradients are 10–50 km wide. We calculate 1-D reflectivity synthetics (Fuchs & Müller 1971; Müller 1985) for *P*-wave periods of 1–10 s, thus covering the range from short period to intermediate period *PP* waves. We aim to use the dominant frequencies and the quarter wavelength criterion to infer the thickness of the reflector using systematic filtering with highpass filters and bandpass filters with narrow passbands. We also try FFT for estimating spectra. However, time windows are too short to give reasonable frequency resolution, and we want to avoid biases from other phases like top-side reflections (e.g. $Pp_{410}p$).

Our tests show that amplitude–frequency curves using highpass filtering do not give constraints (e.g. –3 or –6 dB point of maximum amplitude) which might be converted to reflector thickness. Using our approach with bandpass filtering, we observe that the amplitude–frequency curves do not differ enough for gradients thinner than 20 km in order to discriminate between the different gradient types and to discriminate between a first-order discontinuity and 10–20 km wide gradients. Amplitude–frequency curves for gradients wider than 20 km get more unique shapes. However, mineral physics experiments indicate that the olivine–wadsleyite phase transition and the dissociation of ringwoodite give seismic discontinuities with thicknesses of 6–13 km (e.g. Katsura *et al.* 2004) and 2–6 km (e.g. Litasov *et al.* 2005a), respectively. These

thicknesses cannot be recovered by our approach. We consider forward modelling of each event to constrain the reflector thickness which we have not carried out in this study.

Our analysis results in 68 events with *PP* precursor arrivals and 36 events with *SS* precursor arrivals off upper-mantle and mantle transition discontinuities, with some events showing one *PP* or *SS* precursor arrival and some events with showing several *PP* or *SS* precursor arrival (Fig. 5 and Table S2). The majority of the reflection points are located in Western China between the Tien Shan mountain chain and Eastern Tibet, mirroring the large number of events from the subduction zones ranging from of Sumatra to the Banda Sea which were recorded at seismic stations in Central Europe (Fig. 2). The number of observed *PP* and *SS* underside reflections is sparse along the plate boundary between India and Eurasia.

We observe clear $P^{410}P$ in 53 and $S^{410}S$ in 20 events. The 410 km discontinuity occurs at an average depth of 416 ± 18 km (Fig. 5b) but the detailed topography of the resolved discontinuity is complex and locally shows short-scale topography. The majority of reflections in Tibet and Western China show deep reflections off the 410 km discontinuity, with the deepest reflection at 440 km. The shallowest reflection can be found at a depth of 380 km beneath the Tien Shan and the Himalayas north of Bangladesh.

We observe 31 reflections at depths ranging from 640 to 760 km. Nine of these are observed with *PP* underside reflections, while 22 reflections are observed as *SS* underside reflections. Since the reflections have a wide range of depths, we divide the reflections into two categories: (i) reflections above 700 km depth (Fig. 5d) and (ii) reflections below 700 km depth (Fig. 5e). We separate the reflections into these two categories because the dissociation of ringwoodite is expected to occur at depths shallower than 680 km (e.g. Fei *et al.* 2004). Reflectors deeper than 700 km should be attributed more likely to the garnet to perovskite phase transition which should occur at ∼720 km depth (e.g. Stixrude 1997). The majority of the reflections off the 660 km discontinuity are located under Northern Tibet and the eastern part of the Tarim basin, showing a patch of deep reflections neighboured by shallower reflections. Three reflections off the 660 km discontinuity are located close to the boundary of the Eurasian and Indian plates. We observe isolated reflections off a reflector at an average depth of 720 km depth beneath Northern Tibet and Western China, with individual values ranging from 700 to 740 km.

Apart from observations attributed to major mantle transition zone discontinuities, we detect 10 underside reflections at ∼300 km depth (Fig. 5a) and eight reflections at ∼520 km depth (Fig. 5c). They are observed for shallow events with depths of 10–25 km and are not attributed to depth phases of underside reflections off the 410 or 660 km discontinuity. Seven events sample a region around 40°N, 90°E in northern Tibet. Their reflection depths increase from 300 to 320 km from the northeast to the southwest. We find three additional reflections at 300 km depth beneath central Tibet and close to the plate boundary of Eurasia and India beneath Pakistan. The reflections at ∼520 km (Fig. 5c) have an average depth of 510 ± 21 km.

The vertical cross-sections in Fig. 6 show the lateral variations of the discontinuity depths beneath India and Western China for four different profiles together with recent *P* and *S* tomographic models for the region. Reflection points which are within 1.5° distance of the profiles are included in the cross-sections. Cross-sections A–A′ and B–B′ cut through our investigation region in S–N direction (Figs 6a and b), cross-sections C–C′ and D–D′ in W–E direction (Figs 6c and d). We densely map underside reflections near 410 km depth along the profiles and observe short-scale lateral depth variations. Beneath Eastern India, we observe slightly deeper $P^{410}P$ reflection depths, elevated north of the boundary between the Indian and Eurasian Plate. The deeper $P^{410}P$ reflections are located in regions with positive *P*-wave velocity anomalies (Figs 6a and b). The overlay of discontinuity depths with the cross-sections through the *S*-wave tomography does not indicate correlations of $S^{410}S$ reflector depth with the sign of shear velocity perturbations. Further north, reflection depths for $P^{410}P$ and $S^{410}S$ arrivals appear to deepen and we observe *PP* and *SS* underside reflections off a reflector near 660 km depth. The reflections range between 680 and 740 km depth in northern Tibet and are elevated towards the north end of the profiles A–A′ and B–B′. We observe intermittent reflectors at 300 and 520 km depth beneath the Tibet plateau and North China. The cross-section C–C′ (Fig. 6c) also shows the intermittent reflectors near 300 and 520 km depth. The reflections off the 660 km discontinuity in Western China are observed in a region with positive *P*-wave velocity perturbations.

We do not use amplitudes from vespagrams or amplitude depth profiles from migrations because the major part of *PP* and *SS* precursor arrivals are clearly separated from direct and secondary phases of P/P_{diff}, S/S_{diff} or core phases only when stacked with the 4th root stacking scheme (Davies *et al*. 1971; Muirhead & Datt 1976). The nonlinear 4th root stacking scheme does not preserve amplitudes and therefore makes amplitudes a problematic measurement in those stacks. However, waveform polarities are preserved during non-linear stacking schemes and can be used for further analyses (Rost & Thomas 2002).

5 THERMODYNAMIC MODELLING

We compare the observed discontinuity structure with predicted depths of phase transitions and mineral reactions calculated with Perple_X (Connolly 2005) (see Fig. S1a) which utilizes the free-energy minimization algorithm by Ita & Stixrude (1992) and Stixrude & Lithgow-Bertelloni (2005). We calculate phase equilibria on a grid of pressures and temperatures for the CFMAS (calcium oxide, iron(II) oxide, magnesium oxide, aluminum oxide and silica) system for pyrolite, piclogite, harzburgite and mid ocean ridge basalt (MORB) compositions (Table S3). Pyrolite is the bulk mantle composition which upon partial melting will create MORB oceanic crust and harzburgitic lithosphere (Ringwood 1969), and is frequently assumed to represent the average chemical composition of at least the upper mantle (Weidner 1985; Ita & Stixrude 1992; Jackson & Rigden 1998). We include the piclogite composition by Ita & Stixrude (1992), since Bass & Anderson (1984) and Duffy & Anderson (1989) claim better fits to the seismic constraints of the 410 km discontinuity for a piclogitic mantle composition than for a pyrolitic mantle composition. For the mineral elastic parameters and phase equilibria, we utilise the self-consistent database of Stixrude & Lithgow-Bertelloni (2011). We calculate profiles of *P*-wave velocity, *S*-wave velocity and density for a range of adiabatic mantle geotherms (Fig. S1b) for our chosen chemical mantle compositions. The adiabatic mantle geotherms are calculated as described by Cobden *et al.* (2008). The values of *P*-wave velocity, *S*-wave velocity and density of the phase assemblage at a specific point of pressure and temperature are calculated as the Hill average of the Voigt and Reuss bounds of elastic properties for the constituent minerals (Voigt 1928; Reuss 1929; Hill 1965).

We test the sensitivity of density and wave velocities to bulk composition of our models by calculating phase equilibria for alternative bulk compositions of harzburgite, MORB, piclogite and

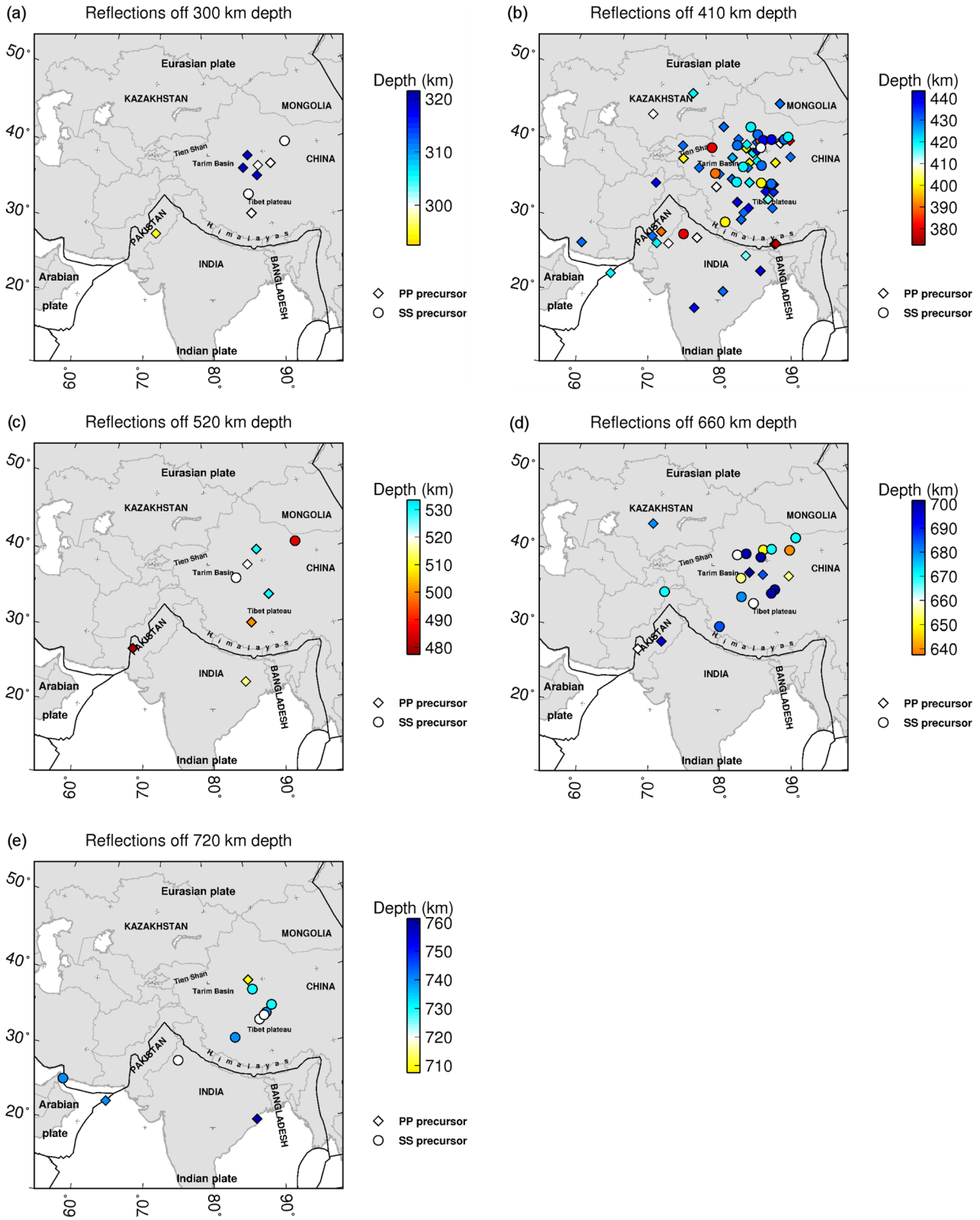

Figure 5. Detections of *PP* and *SS* underside reflections and their measured reflection depths. The depth is colour-coded. Shallower reflection depths are indicated by red colours, deeper reflection depths are indicated by blue colours. Plate boundaries are from Bird (2003). (a) Depth observations of reflections around 300 km depth. (b) as (a) but for depths around 410 km. (c) As (a) but for depths around 520 km. (d) As (a) but for depths around 660 km. (e) As (a) but for depths around 720 km. The error in observed discontinuity depth is ±8 km, which we have derived from resolution tests of the migration scheme and from migrations with and without traveltime corrections.

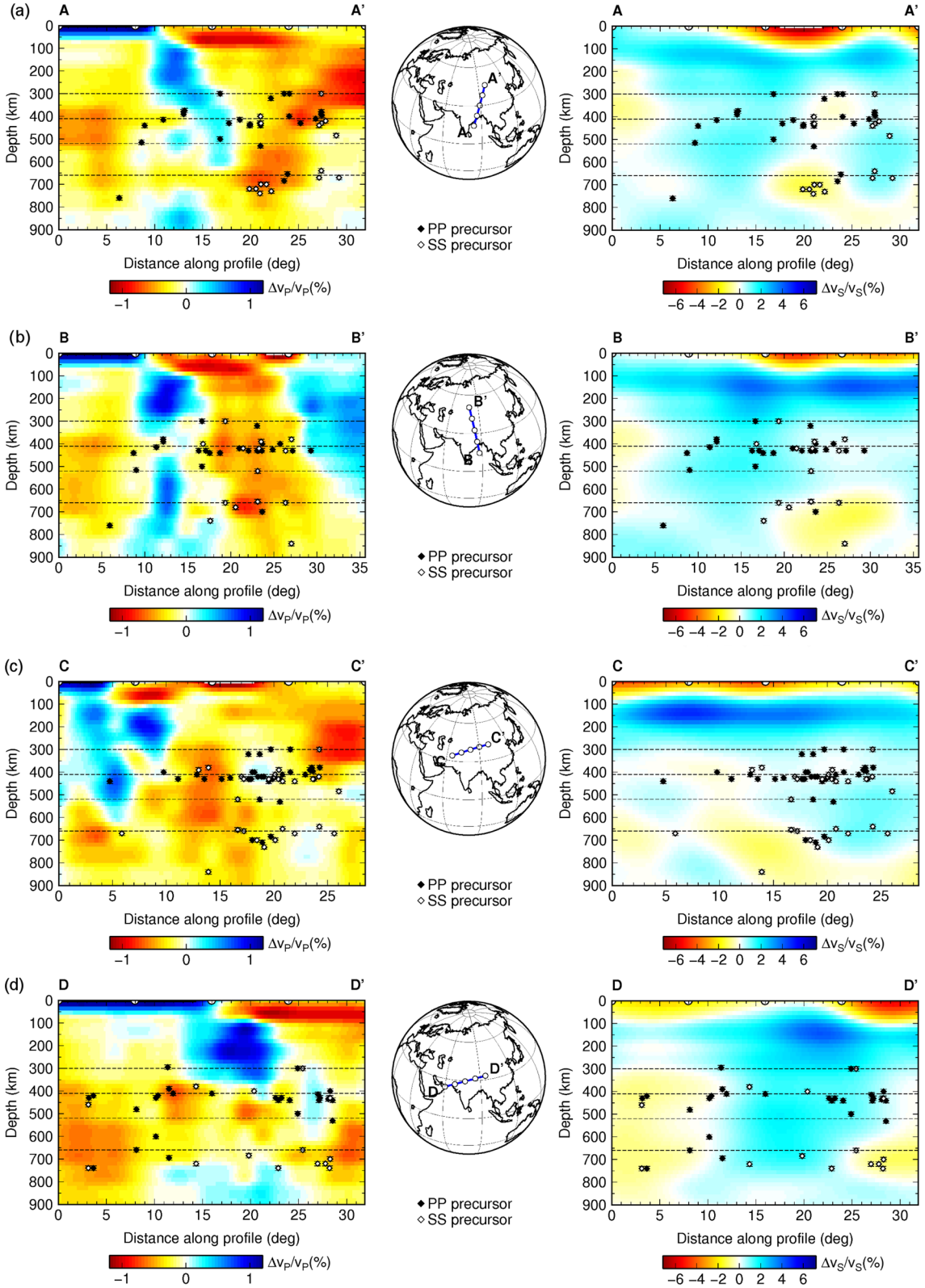

Figure 6. Observations of *PP* and *SS* underside reflections (diamonds) beneath India and Western China, superimposed on the *P*-wave tomographic model MITP08 (Li *et al.* 2008) (left) and on the *S*-wave tomographic model S40RTS (Ritsema *et al.* 2011) (right) along selected profiles through the investigation region (centre). Reflection points which lie within 1.5° distance of a profile are included in the cross-sections. The discontinuity depths measured from the migration of each event are indicated by diamonds, where open diamonds depict *P*-wave measurements and black diamonds *S*-wave measurements. Horizontal lines indicate depths of 300, 410, 520 and 660 km. The location of each profile is marked on the globe adjacent to each vertical cross-section; circles on the profile are also indicated at the top of the cross-sections. (a) Cross-section from A to A′. (b) Cross-section from B to B′. (c) Cross-section from C to C′. (d) Cross-section from D to D′.

pyrolite published in the literature (Green *et al.* 1979; Ringwood 1979; Sun 1982; Bass & Anderson 1984; Michael & Bonatti 1985; Irifune & Ringwood 1987; Irifune & Ringwood 1993; McDonough & Sun 1995; Hofmann 1988; Baker & Beckett 1999; Ono *et al.* 2001, 2005; Litasov *et al.* 2004; Hirose *et al.* 2005; Workman & Hart 2005; Perrillat *et al.* 2006; Ricolleau *et al.* 2010). We find negligible differences in densities and wave velocities among alternative pyrolite compositions for a fixed adiabatic geotherm. The depths of the transformation could be shifted within ∼4 km. The absolute increases in density and wave velocities as well as the shape of these increases and the transformation depth interval are not significantly affected.

There are no large variations in the wave velocity and density profiles among harzburgite compositions. Differences in profiles of density and wave velocities among alternative harzburgite compositions arise from different iron(II) oxide contents which affect the transformation depth interval of the seismic discontinuity caused by the olivine to wadsleyite phase transition. The olivine–wadsleyite phase transition is shifted to deeper depths (∼5 km), whereas the dissociation of ringwoodite is elevated towards shallower depths (∼2 km), compared with the pyrolite composition. In addition, the transformation intervals are smaller than for pyrolite composition, leading to sharper seismic discontinuities.

In MORB compositions, there are no mineral transformations for the depth range of the mantle transition zone. However, there are two seismic discontinuities at approximately 300 and 750 km depth, corresponding to the phase transition of coesite to stishovite (Williams & Revenaugh 2005) and garnet to perovskite (Hirose 2002). Among MORB compositions, there are broader variations in the oxides (e.g. Deschamps *et al.* 2012). The profiles of density and wave velocities have similar slopes between transformations for a fixed geotherm. The garnet to perovskite phase transition occurs at similar depths with variations of ∼4 km. Differences in the proportions of the oxides, however, change the seismic structure of the garnet to perovskite phase transition for a given geotherm (Fig. S4).

We measure the depth and the depth interval of the mineral transformations from the calculated seismic profiles as well as the change in density, *P*- and *S*-wave velocity across the mineral transformations. In order to interpret our seismic observations using the calculated mineral physical models, we compare the depths of the observed underside reflections with the depths of mineral transformations, assuming an uncertainty of 0.6 GPa for the transformation pressure (Smyth & Frost 2002), that is, a depth uncertainty of ±14 km, for a fixed composition and temperature. We interpret lateral variations in discontinuity depths in terms of deviations with respect to a reference model corresponding to a pyrolitic composition and 1300 °C adiabatic temperature profile whose zero-pressure temperature of 1300 °C is sufficient to explain the 1-D seismic reference models PREM or ak135 (Weidner 1985; Ita & Stixrude 1992; Jackson & Rigden 1998).

6 INTERPRETATION AND DISCUSSION

6.1 The 300 km discontinuity

Observations of seismic reflections from 300 to 320 km depths (Fig. 5a) may be due to the X-discontinuity that has been attributed to the exothermal phase transition of coesite to stishovite (Williams & Revenaugh 2005). In our Perple_X calculations, this sharp phase transition is expected to occur for pressures between 8 and 11 GPa, that is, 250 and 320 km, in MORB mantle chemistry (Fig. 7a). The X discontinuity has been used to constrain the presence and amount of subducted or delaminated, formerly basaltic material in the upper mantle and to map regions of ancient subduction (Williams & Revenaugh 2005).

Another possible explanation for a seismic discontinuity between 300 and 320 km depth could be the exothermic mineral transformation in calcium-poor pyroxene from ortho-enstatite (cpx) to high-clinoenstatite (c2/c) occurring at depths of 250–330 km (Mendelssohn & Price 1997; Woodland & Angel 1997). Based on the calculated seismic velocities we find that plane wave *PP* and *SS* underside reflection coefficients (Aki & Richards 1980) off the seismic discontinuity caused by the ortho-enstatite to high-clinoenstatite are an order of magnitude smaller than the reflection

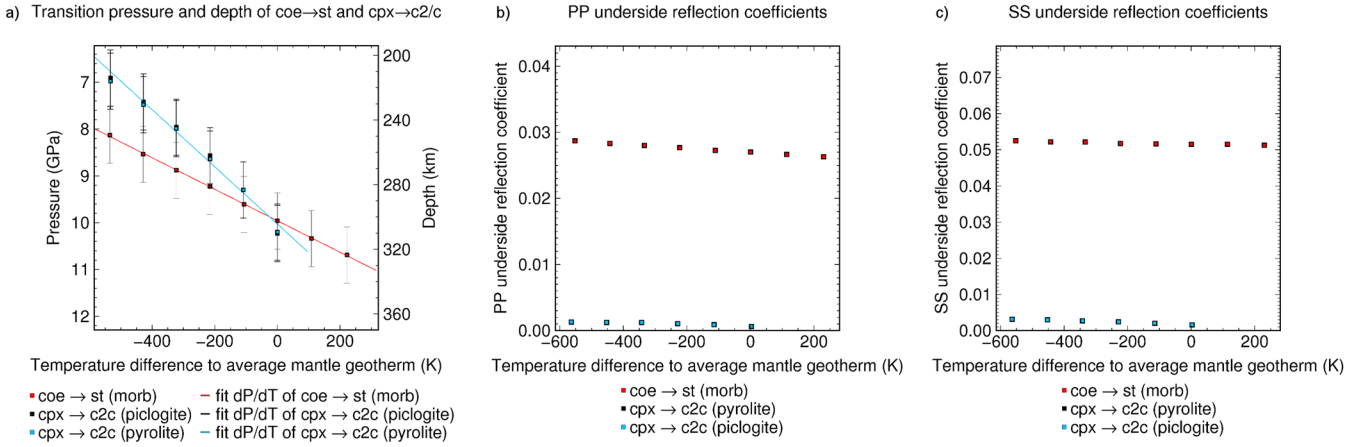

Figure 7. Transition pressure and depth and *PP* and *SS* underside reflection coefficients for mineral transformations around 300 km depth from thermodynamic calculations with Perple_X. (a) Transition pressure and depth of the coesite (coe) to stishovite (st) phase transition for MORB composition and of the clinopyroxene (cpx) to high-pressure pyroxene (c2/c) mineral transformation of pyrolite and piclogite composition. The error bars indicate a pressure uncertainty of 0.6 GPa (Smyth & Frost 2002). The Clapeyron slopes of the mineral transformations are fit as the linear regression of the transition pressures. For temperatures warmer than given by the 1300 °C adiabat around ∼300 km depth, our thermodynamic calculations do not show a discontinuous increase of wave velocities and density for the clinopyroxene (cpx) to high-pressure pyroxene (c2/c) mineral transformation of pyrolite and piclogite composition. (b) *PP* underside reflection coefficients as a function of temperature difference with respect to the average mantle geotherm for a distance of 100°. (c) *SS* underside reflection coefficients as a function of temperature difference with respect to the average mantle geotherm for a distance of 100°.

coefficients off the seismic discontinuity caused by the coesite to stishovite phase transition for our distance range (Figs 7b and c). We therefore consider it unlikely that the mineral transformation from ortho-enstatite to high-clinoenstatite would be a cause of underside reflections at 300 km depth.

The X-discontinuity has been observed in several seismic studies (e.g. Revenaugh & Jordan 1991; Deuss & Woodhouse 2002). The six reflections which we observe at ∼300 km depth in northern Tibet can perhaps be attributed to subducted remnants of the collision of Eurasia with Tibet during the late Triassic, early Jurassic (∼200 Ma) when Eurasian lithosphere was subducted in a southward direction (Willet & Beaumont 1994; Tapponnier *et al.* 2001; Haines *et al.* 2003). Kind *et al.* (2002) and Zhao *et al.* (2011) observe a southward dipping interface in *P*- and *S*-wave receiver functions for the northern part of the Tibetan plateau. The reflector appears to deepen from 300 to 320 km depth from north to south. The deepening of the reflector could be related to increasing temperature from north to south of –250 to +100 K with respect to the 1300 °C potential temperature mantle geotherm (Fig. 7a). Given the uncertainties of the depth measurements, our observations could also be reconciled with a flat reflector.

6.2 The 410 km discontinuity

Reflections off the 410 km discontinuity appear deepest in Western China (Fig. 5) close to decreased *P*-wave velocity anomalies in the tomography sections (Fig. 6). This correlation could be due to increased mantle temperatures (Fig. S3a). Since the Clapeyron slope of the olivine to wadsleyite phase transition is positive, increased mantle temperatures shift the phase transition to higher pressures, that is, to deeper depths. The deepest reflections would correspond to temperature differences of 100–200 K with respect to the average mantle geotherm, values appropriate to estimates for excess temperatures in mantle upwellings (e.g. Sleep 1990). Our observations are supported by the study of Kosarev *et al.* (1999) who observe a complex pattern of locally elevated and discontinuous *P* to *S* conversions at the 410 km discontinuity beneath the Tibet plateau. Kosarev *et al.* (1999) suggest that upwelling mantle material is a response to the subducting Indian lithosphere. However, the *S*-wave tomographic models do not show short-scale *S*-wave velocity anomalies at the same locations (Fig. 6).

For the reflections beneath the Tien Shan and the Himalayas north of Bangladesh, we observe elevated reflections of the 410 km discontinuity. The reflection points are close to plate boundaries and regions of ongoing subduction (Yin & Harrison 2000). Possibly, these elevated reflections of the 410 km discontinuity could be related to cold, subducting lithosphere reaching the top of the mantle transition zone. The *P*-wave tomographic model MITP08 shows regions of increased *P*-wave velocity anomalies that Li *et al.* (2008) interpret as Indian lithosphere subducting northward beneath Tibet and bending down into the mantle transition zone. Due to the positive sign of the Clapeyron slope, colder temperatures shift the olivine to wadsleyite phase transition to lower pressures, that is, shallower depths. The elevated reflections off the 410 km discontinuity correspond to maximum temperature differences of 200–400 K colder relative to the average mantle geotherm (Fig. S3a).

Our thermodynamic modelling does not account for the influence of water on phase equilibria. The presence of water could affect the physical properties of the mantle rocks (e.g. Hirschmann 2006). Water can occur in mantle rocks and minerals as a constituent part of minerals (e.g. Poli & Schmidt 2002) or incorporated in minerals with low water solubility such as olivine (e.g. Kohlstedt *et al.* 1996). One potential source of water for mantle minerals is the subduction of oceanic lithosphere that has been hydrated through normal faults before subduction (Ranero *et al.* 2003). Mineral physical experiments suggest that wadsleyite and ringwoodite have larger water storage capacities than olivine (e.g. Kohlstedt *et al.* 1996; Ohtani *et al.* 2000) as well as magnesium perovskite and magnesiowuesite (Litasov *et al.* 2003; Litasov 2010). Based on these results, Bercovici & Karato (2003) hypothesize that wadsleyite and ringwoodite may store significant amounts of water and that the local water content may affect the structure and dynamics of the mantle.

The presence of hydrous minerals could reduce *P*- and *S*-wave velocities in the mantle transition zone (e.g. Chen *et al.* 2002; Wang *et al.* 2003; Jacobsen *et al.* 2004; Sanchez-Valle *et al.* 2006, 2008; Mao *et al.* 2008, 2010; Li *et al.* 2009). When upwelling mantle crosses the olivine to wadsleyite phase transition depth, water has to be released due to the different storage capacities. At 1500 °C, the release of water could lead to a hydrous partial melt which would trap incompatible trace elements. The presence of partial melt could lead to a drop of seismic wave velocities in the melt while seismic wave velocities remain larger outside the molten rock. The partial melt on top of the 410 km discontinuity could enhance the amplitude of the $P^{410}P$ or $S^{410}S$ precursor and be followed by a secondary reflection from the top of the melt lens with a negative polarity. Depending upon the thickness of the melt lens, these two reflectors might interfere constructively and enhance the sidelobe of the $P^{410}P$ or $S^{410}S$ precursor, giving it the appearance of a negative polarity. Nonetheless, these are two separate arrivals, one with a positive and a second later one with a negative arrival (Revenaugh & Sipkin 1994; Song *et al.* 2004; Schmerr & Garnero 2007; Thomas & Billen 2009). In our data set, however, we do not observe *PP* or *SS* underside reflections with apparently reversed polarities, likely indicating the absence of partial melt on top the 410 km discontinuity.

6.3 The 520 km discontinuity

We observe an intermittent seismic discontinuity near 520 km depth (Fig. 5c). A discontinuity at 520 km depth coincides with the wadsleyite to ringwoodite phase transition (Suzuki *et al.* 2000). It has been detected in some regions of the mantle and is assumed to be a regional feature (e.g. Shearer 1990; Ryberg *et al.* 1998; Gu *et al.* 1998; Deuss & Woodhouse 2001). Underside reflections off 520 km depth are apparently absent beneath continental shield regions, but have been observed under oceans (Deuss & Woodhouse 2001; Thomas & Billen 2009). Deuss & Woodhouse (2001) and Thomas & Billen (2009) observe split arrivals of *PP* and *SS* underside reflections with depths of 450–500 and 540–560 km.

Saikia *et al.* (2008) suggest that the exsolution of calcium–silicate perovskite from garnet can produce a sharp seismic reflector in the mid-transition zone. This transition occurs at 19–20 GPa corresponding to a deeper reflector around 560 km over a depth interval of 40–60 km. The major part of the transition occurs within the top 10–20 km, leading to an impedance contrast of 0.5–1.0 per cent over 20 km (Saikia *et al.* 2008).

In our Perple_X calculations, we do not observe discontinuous increases or strong gradients in seismic properties caused by the mineral transformation of clinopyroxene/garnet to calcium perovskite and garnet for the phase equilibria calculation for pyrolite, harzburgite or MORB compositions (Figs S2 and S3). Only for the piclogite composition and geotherms with potential temperatures between 800 and 1000 °C, we find discontinuous increases in seismic properties caused by the exsolution of calcium perovskite, occurring at temperatures of 400–600 K colder relative to

average mantle geotherms (Fig. S3b). For the remaining geotherms, we observe smooth wave velocity and density variations instead of discontinuities. However, available data on element partitioning have significant influence on the detailed seismic structure across phase boundaries. Based on the database of elastic properties and the solid-solution model by Stixrude & Lithgow-Bertelloni (2011), our observations of single reflectors at 490–530 km depth are more consistent with the wadsleyite to ringwoodite phase transition as discussed by Saikia *et al.* (2008), with temperatures between average mantle temperature and up to 400 K colder than the average mantle temperature (Fig. S3b).

6.4 The 660 km discontinuity

We observe single *PP* and *SS* underside reflections off depths around 660 km spread over the entire investigation area and an accumulation of *PP* and *SS* underside reflections off 640–740 km depth beneath Tibet and Northern China (Figs 5d,e and 6). We have more non-detections than detections of $P^{660}P$ and $S^{660}S$. In previous studies undertaken in various regions of the Earth, stacks of underside reflected *PP* and *SS* waveforms generally show robust detections of $P^{410}P$, $S^{410}S$ and $S^{660}S$, while $P^{660}P$ is frequently absent (Estabrook & Kind 1996; Rost & Weber 2002; Deuss 2009). Deuss *et al.* (2006), Thomas & Billen (2009) and Schmerr & Thomas (2011) show complex patterns of $P^{660}P$ detections and non-detections. Non-detections of $P^{660}P$ can be generated by lower density and velocity jumps at 660 km depth than in PREM or IASP91 (Estabrook & Kind 1996; Shearer & Flanagan 1999). The changes of density and velocity jumps of these models at 660 km depth have a similar order of magnitude indicated by recent thermodynamic modelling (e.g. Vacher *et al.* 1998; Cobden *et al.* 2008).

Four factors can contribute to non-observations of *PP* and *SS* underside reflections: (i) interference with other seismic phases, (ii) destructive interference of reflections off two closely spaced reflectors, (iii) wavefield focusing or defocusing due to non-planar or inclined reflectors (Neele & Snieder 1992; Neele *et al.* 1997; Chaljub & Tarantola 1997) and (iv) the sharpness of the discontinuities. Interfering seismic phases, for example, source-side or receiver-side reflections and conversions arriving after the P/P_{diff}, S/S_{diff} arrivals and with similar horizontal slowness values, may hinder observations for a distance range of 90–115° (e.g. Shearer 1991; Schmerr & Garnero 2006; Deuss 2009). Side lobes of the slant stacked arrivals of source-side or receiver-side reflections and conversions could destructively interfere and obscure *PP* and *SS* underside reflections off the 410 or the 660 km discontinuity. Destructive interference could also produce a null observation at the 660 km discontinuity, if the depth spacing of the reflectors causes the sidelobes of the precursory reflections to overlap deconstructively in time.

The topography of a reflector can lead to focusing or defocusing of the *PP* and *SS* wavefield and complicate measurements of reflection depth, amplitude and waveform (Neele & Snieder 1992; Chaljub & Tarantola 1997; Neele *et al.* 1997). Deflections of the 660 km discontinuity to deeper depths could focus seismic energy and increase the amplitude of the underside reflection by 50 per cent. Deflections of the 660 km discontinuity to shallower depths could defocus seismic energy and decrease the amplitude of the underside reflection by 50 per cent (Chaljub & Tarantola 1997). Underside reflections of the 660 km discontinuity have been observed in regions of positive wave velocity anomalies in seismic tomography models, and have been interpreted as subducting slabs impinging on the bottom of the mantle transition zone (e.g. Deuss 2009; Thomas & Billen 2009; Schmerr & Thomas 2011). However, observations of $P^{660}P$ are scarce away from subducting slabs (Deuss 2009; Thomas & Billen 2009; Schmerr & Thomas 2011). The 2.5-D or 3-D modelling of $P^{d}P$ and $S^{d}S$ waveforms and their detection with array seismic methods is beyond the scope of this paper. Recent waveform modelling studies demonstrate the significance of considering topography on seismic reflectors in the mantle (e.g. Bai *et al.* 2012; Zheng & Romanowicz 2012; Hempel *et al.* 2013).

The *P*- or *S*-wave impedance contrast or the reflector thickness could affect the detectability of *PP* and *SS* underside reflections. Estabrook & Kind (1996) suggest a modified version of IASP91 (Kennett & Engdahl 1991) with 50 per cent reduced *P*-wave velocity contrast at 660 km depth. This leads to low *PP* underside reflection coefficients over the distance range used in their global *PP* precursor stacks. Shearer & Flanagan (1999) give an additional model with a comparable *P*-wave impedance contrast at 660 km depth. Rost & Weber (2002) investigate a range of 1-D earth models for non-observations of $P^{660}P$ for short-period (1 s) *PP* waves, and find that if the *P*-wave impedance jump is less than 9 per cent for a sharp discontinuity, or that the discontinuity is thicker than 12 km, then $P^{660}P$ cannot be detected.

Based on the synthetic seismic profiles computed in this study, we find that, for a variety of compositions and geotherms, plane wave *PP* and *SS* underside reflection coefficients at ∼660 km depth are sensitive to the incidence angle and hence epicentral distance between source(s) and receivers. We compare these results with *PP* and *SS* underside reflections of the 660 km discontinuity of PREM (Dziewonski & Anderson 1981) and ak135 (Kennett *et al.* 1995; Fig. 8) since these models can represent over 90 per cent of the global seismic data (e.g. Cobden *et al.* 2008). PREM and ak135 are globally averaged models which can be reasonably explained by the seismic properties of pyrolitic mantle composition following the adiabatic 1300 °C potential temperature geotherm (Weidner 1985; Ita & Stixrude 1992; Jackson & Rigden 1998). However, there is evidence for bias of these models due to 3-D structural heterogeneity, for example, subducting slabs (e.g. Cammarano *et al.* 2005; Cobden *et al.* 2008).

Using a pyrolite composition and the temperature profile of a 1300 °C adiabat, we observe that *PP* underside reflection coefficients have a minimum within our distance range of 85–115°. The reflection coefficients are significantly smaller than those of the 660 km discontinuity in PREM and ak135 for all incidence angles (Fig. 8a). Reflection coefficients of *SS* precursors show a higher sensitivity to incidence angle, and hence epicentral distance, than *PP* precursors, with a strong increase in amplitude for epicentral distances larger than 100° (Fig. 8b). We observe similar patterns for the distance-dependence of $P^{660}P$ and $S^{660}S$ underside reflection coefficients for other combinations of compositions and mantle temperatures.

The distance-dependent behaviour of reflection coefficients at seismic discontinuities at ∼660 km differs from the distance-dependent behaviour at the 410 km discontinuity. We find that the 410 km *PP* and *SS* underside reflection coefficients are less sensitive to incidence angle (i.e. distance) than at 660 km depth, for both our set of thermochemical models and the seismic reference models PREM and ak135 (Figs 8c and d). Reflection coefficients for the olivine to wadsleyite phase transition range from 2 to 2.5 per cent for *PP* waves, and 2.5 to 4 per cent for *SS* waves, with similar values for ak135. For PREM the reflection coefficients are around 1.5 per cent for *PP* waves, and range between 1 and 1.8 per cent for *SS* waves. The dependence of the *PP* and *SS* underside reflection coefficients on the incidence angle for the 660 km discontinuity could be an

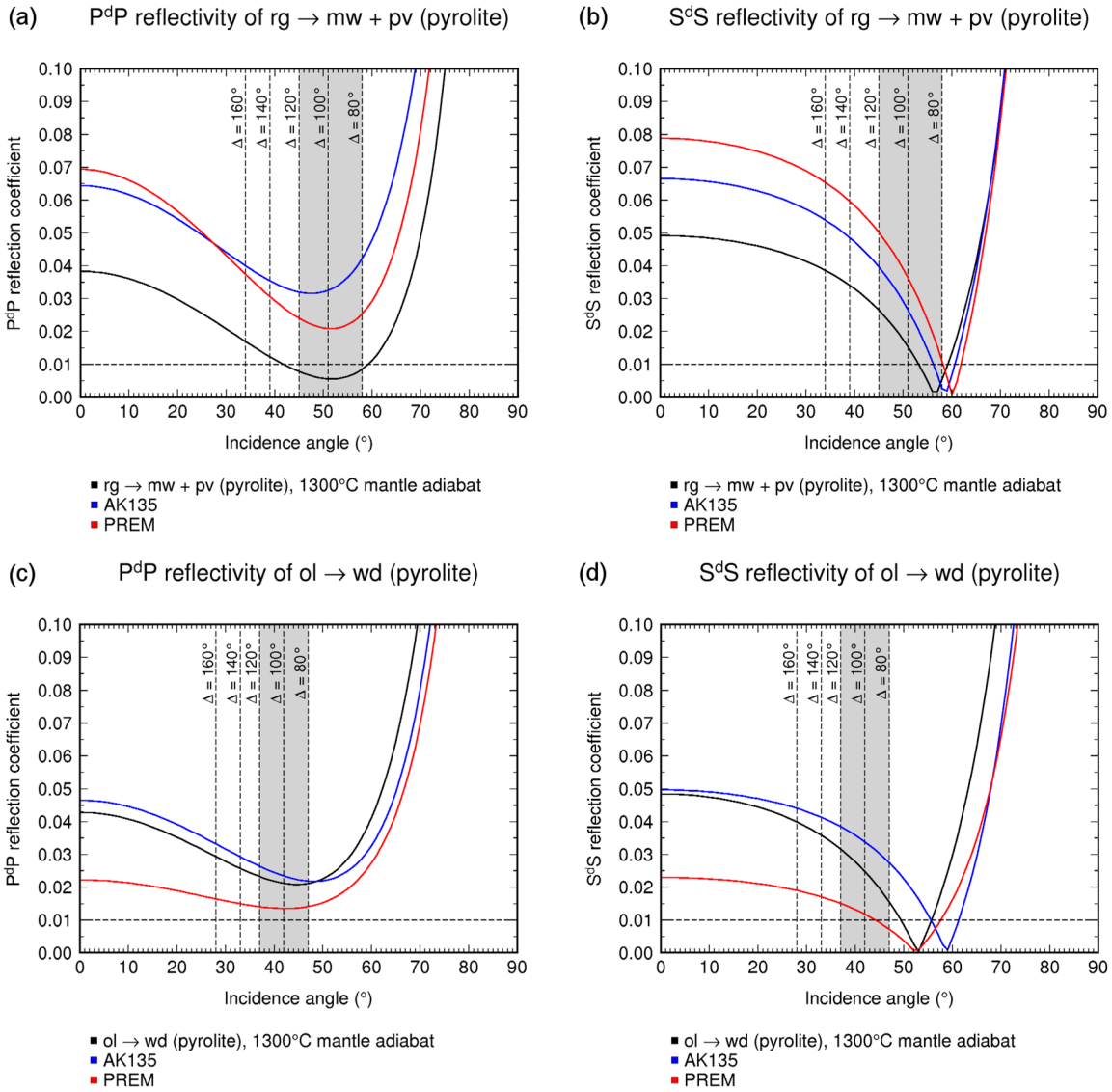

Figure 8. Comparison of *PP* and *SS* underside reflection coefficients for the seismic discontinuity caused by the dissociation of ringwoodite (rg) to magnesiowuestite (mw) and perovskite (pv) and for the seismic discontinuity caused by the olivine (ol) to wadsleyite (wd) phase transition. The reflection coefficients are calculated for increases of density, *P*- and *S*-wave velocity for pyrolite mantle composition, following the 1300 °C potential temperature adiabat. *PP* and *SS* underside reflection coefficients for PREM (Dziewonski & Anderson 1981) and ak135 values for jumps of the density, *P*- and *S*-wave velocity at the 660 km discontinuity are plotted for comparison. Vertical dashed lines indicate incidence angles at a plane reflector for the given epicentral distances. The available distance range of this study is indicated by the grey-shaded area. (a) *PP* underside reflection coefficient as the function of the incidence angle for the seismic discontinuity caused by the dissociation of ringwoodite (rg) to magnesiowuestite (mw) and perovskite (pv). (b) *SS* underside reflection coefficient as the function of the incidence angle for the same seismic discontinuity in (a). (c) *PP* underside reflection coefficient as the function of the incidence angle for the seismic discontinuity caused by the olivine (ol) to wadsleyite (wd) phase transition. (d) *SS* underside reflection coefficient as the function of the incidence angle for the same seismic discontinuity in (c).

additional contribution to the mechanisms causing non-observations of $P^{660}P$ and $S^{660}S$. However, since we do not observe a systematic change in the visibility of the reflections as a function of epicentral distance this cannot be the dominant factor involved.

Beneath Tibet and Western China, we observe *PP* and *SS* underside reflections at ∼700–740 km depth, which apparently bend downward in the cross-sections A–A′ and C–C′ (Figs 6a and c). Given a maximum uncertainty of ±8 km on the inferred reflector depths, these reflectors clearly lie deeper than 660 km. One explanation of these observations could be the presence of a seismic discontinuity associated with the garnet to perovskite phase transition. This interpretation for deep reflectors has previously been suggested by Deuss *et al.* (2006) beneath Canada and Greenland, by Cao *et al.* (2010, 2011) beneath the Northern Pacific and by Day & Deuss (2013) beneath East Africa. If these reflectors would be due to thermal effects of the garnet to perovskite phase transition only, the reflector depths would correspond to a temperature difference of –600 to –150 K with respect to the average mantle geotherm using our Perple_X calculations (Fig. S3c). However, note that the garnet to perovskite transition has one of the least constrained Clapeyron slopes among the mineral transformations of the mantle transition zone. Slopes between +2 to +6 MPa K^{-1} have been reported (Cao *et al.* 2011 and references therein). The garnet to perovskite phase transition may occur over a broad depth range of ∼100 km.

However the finalisation of the garnet to perovskite phase transition for MORB, pyrolitic and piclogitic compositions occurs within a narrow depth range of ∼ 2 km, thus giving rise to discontinuous jumps of wave velocities and density in our calculations (Figs S3c,d and f; Fig. S4). Note that harzburgite does not have a garnet to perovskite phase transition, due to its aluminum depletion.

A possible mechanism for garnet enrichment at these depths is subducted garnet-rich crust, which can be segregated from the underlying oceanic lithospheric mantle during subduction, and is neutrally buoyant beneath the mantle transition zone (Ringwood 1967; Anderson 1979; Ringwood & Irifune 1988; Karato 1997; Lee & Chen 2007): Major parts of the basaltic oceanic crust transform into eclogite at ∼40 km depth (e.g. Stern 2000) and a thin layer of serpentinite may act as a weak zone between lithospheric mantle and eclogitized oceanic crust (e.g. Stern 2000; Poli & Schmidt 2002). Due to higher density of the eclogitized oceanic crust compared to the underlying lithospheric mantle, shear stresses may segregate oceanic crust from the lithospheric mantle along the serpentinite layer. The eclogitized mineral assembly undergoes phase transitions into a garnet-rich assembly (garnetite) between 400 and 800 km depth and becomes buoyant between 660 and 800 km depth. We find relative density differences of –1 to –4 per cent between MORB and pyrolite between 660 and 800 km depth in our thermodynamic calculations. Lee & Chen (2007) suggest that patches of garnetite material may then accumulate beneath the 660 km discontinuity, leading to a garnet rich zone and reflectors at ∼660–800 km depth. In our study region, the source for oceanic crust residing below the mantle transition zone north of Tibet could be remnants of crust of the Tethys Ocean between India and the Tibet-forming terranes (Yin & Harrison 2000; Haines *et al.* 2003).

As for the 410 km discontinuity, our thermodynamic modelling does not account for effects of water content on phase equilibria near ∼660 km depth. Water can affect the depth and the thickness of the dissociation of ringwoodite (e.g. Litasov *et al.* 2005b) since it can incorporate a large amount of hydrogen in its structure (e.g. Kohlstedt *et al.* 1996). The incorporation of hydrogen into ringwoodite can expand its stability field to higher pressures compared to the anhydrous system (e.g. Litasov *et al.* 2005b). Experiments by Ghosh *et al.* (2013) in anhydrous and hydrous Mg_2SiO_4 of Fe-free harzburgitic composition show that 2 wt% H_2O results in a shift of the phase boundary from 22.1 GPa to 23.4–23.6 GPa at 1500 K compared with anhydrous Mg_2SiO_4 and hydrous pyrolite. The Clapeyron slope of the dissociation of ringwoodite for hydrous Mg_2SiO_4 decreases to –3.2 to –3.1 MPa K^{-1}, compared to –0.4 to –0.7 MPa K^{-1} for anhydrous Mg_2SiO_4. Hence, increased water content at ∼660 km depth could possibly lead to observations of $P^{660}P$ and $S^{660}S$ underside reflections off deeper depths than for anhydrous systems. Since we observe single reflectors at 660–700 km depth beneath Western China, water bearing ringwoodite could possibly be present at the bottom of the mantle transition zone in this area.

Observations of complicated seismic structure at ∼660 km depth beneath Tibet have also been seen in stacks of broad-band *SS* waveforms (Heit *et al.* 2011) for which a similar combination of sources and receivers was used. The *SS* stacks show complex patterns of $S^{660}S$ reflections on a corridor from Tibet to the Kurile subduction zone near 90°E and 100°E (see figs 8 and 10 in Heit *et al.* 2011). The reflecting surface appears to be discontinuous, with patches of increased reflectivity and showing deflections down to 700 km near 95°E. Additionally, receiver function profiles by Kind *et al.* (2002) also show lateral variations of conversion depths and amplitudes of the P660s signals in the mantle transition zone (see fig. 3b in Kind *et al.* 2002). Between 33°N and 37°N the P660s conversion is underlain by *P*-to-*S* converted energy at 700–750 km depth which coincides with the location of our observations of *PP* and *SS* underside reflections off 700–740 km depth. Hence our observations are compatible with previous studies of the 660 km discontinuity in this region based on independent data sets.

7 CONCLUSIONS

The topography of upper-mantle and mantle transition zone discontinuities beneath India and Western China was imaged using array seismic methods applied to *PP* and *SS* underside reflections. The results show deep reflectors of $P^{410}P$ and $S^{410}S$ from the olivine to wadsleyite phase transition beneath Tibet, Western China and India at depths of 410–440 km depth, elevated to 370–390 km beneath the Tien Shan region and Eastern Himalayas, probably as a response to cold, subducting lithosphere.

The data set contains several non-detections of $P^{660}P$ and $S^{660}S$ underside reflections. From our computed phase equilibria and profiles of seismic velocities and density, we find that the reflectivity off seismic discontinuities at ∼660 km depth is sensitive to incidence angle and has minima within the distance range of our data sets. This indicates that the combination of sources and receivers of this study could be unfavourable for illuminating the detailed structure of the existing discontinuity structure. Nonetheless, we observe deep reflections at 660–700 km depth beneath Northern China where we also observe intermittent *PP* and *SS* underside reflections off ∼520 km depth. We find a deeper reflector between 700 and 740 km depth, that is, below the mantle transition zone, beneath Tibet. These seismic reflectors could be explained by the garnet to perovskite phase transition which could possibly be caused by the presence of MORB material due to segregated oceanic crust beneath Tibet, forming a neutrally buoyant garnet-rich layer at the top of the lower mantle. Our observations of reflectors at ∼700–740 km depth in this region are consistent with previous studies of *SS* waveforms and receiver functions.

ACKNOWLEDGEMENTS

We are grateful for the constructive comments by Dan Shim, Nicholas Schmerr and one anonymous reviewer that helped to greatly improve the quality of the manuscript. The facilities of the IRIS Data Management System, Observatories and Research Facilities for European Seismology (ORFEUS) Data Management Centre and the WebDC Common Data Portal for GFZ Potsdam, German and European Seismological Data Archives were used for access to waveform, metadata or products required in this study. The IRIS-DMS is funded through the National Science Foundation (NSF). The ORFEUS DMC and WebDC are funded by the Network of Research Infrastructures for European Seismology (NERIES) project of European Commission. We thank Jamie Connolly for assistance with the Perple_X program package. Data analyses were carried out with SeismicHandler (Stammler 1993), Seismic Analysis Code (Goldstein *et al.* 2003) and the TauP toolkit (Crotwell *et al.* 1999). Maps and figures were produced with GMT (Wessel & Smith 1995). SL was supported under grant DFG TH1530/2–1. LC was supported under grant DFG TH1530/5–1. The Morocco Münster project is funded under grant DFG TH1530/5–1.

REFERENCES

Aki, K. & Richards, P.G., 1980. *Quantitative Seismology: Theory and Methods,* W. H. Freeman.

Anderson, D.L., 1979. Chemical stratification of the mantle, *J. geophys. Res.-Solid Earth,* **84,** 6297–6298.

Andrews, J. & Deuss, A., 2008. Detailed nature of the 660 km region of the mantle from global receiver function data, *J. geophys. Res.-Solid Earth,* **113,** B06304, doi:10.1029/2007JB005111.

Bai, L., Zhang, Y. & Ritsema, J., 2012. An analysis of *SS* precursors using spectral element method seismograms, *Geophys. J. Int.,* **188,** 293–300.

Baker, M. & Beckett, J.R., 1999. The origin of abyssal peridotites: a reinterpretation of constraints based on primary bulk compositions, *Earth planet. Sci. Lett.,* **171,** 49–61.

Bass, J.D. & Anderson, D.L., 1984. Composition of the upper mantle: geophysical tests of two petrological models, *Geophys. Res. Lett.,* **11,** 229–232.

Bassin, C., Laske, G. & Masters, G., 2000. The current limits of resolution for surface wave tomography in North America, *EOS, Trans. Am. Geophys. Un.,* **81**, F897.

Benz, H.M. & Vidale, J.E., 1993. Sharpness of upper-mantle discontinuities determined from high frequency reflections, *Nature,* **365,** 147–150.

Bercovici, D. & Karato, S., 2003. Whole mantle convection and the transition zone water filter, *Nature,* **425,** 39–44.

Bina, C.R. & Helffrich, G.R., 1994. Phase-transition Clapeyron slopes and transition zone seismic discontinuity topography, *J. geophys. Res.-Solid Earth,* **99,** 15 853–15 860.

Bird, P., 2003. An updated digital model of plate boundaries, *Geochem., Geophys., Geosyst.,* **4,** 1027, doi:10.1029/2001GC000252.

Brandon, C. & Romanowicz, B., 1986. A no-lid zone in the central Chang-Tang platform of Tibet–Evidence from pure path phase-velocity measurements of long period Rayleigh-waves, *J. geophys. Res.-Solid Earth,* **91,** 6547–6564.

Cammarano, F., Goes, S., Deuss, A. & Giardini, D., 2005. Is a pyrolitic adiabatic mantle compatible with seismic data? *Earth planet. Sci. Lett.,* **232,** 227–243.

Cao, Q., Wang, P., van der Hilst, R.D., de Hoop, M.V. & Shim, S.-H., 2010. Imaging the upper mantle transition zone with a generalized Radon transform of *SS* precursors, *Phys. Earth planet. Inter.,* **180,** 80–91.

Cao, Q., van der Hilst, R.D., de Hoop, M.V. & Shim, S.H., 2011. Seismic imaging of transition zone discontinuities suggests hot mantle west of Hawaii. *Science,* **332,** 1068–1071.

Capon, J., 1973. Signal processing and frequency-wavenumber spectrum analysis for a large aperture seismic array, *Method Comp. Phys.,* **13,** 1–59.

Chaljub, E. & Tarantola, A., 1997. Sensitivity of *SS* precursors to topography on the upper-mantle 660-km discontinuity, *Geophys. Res. Lett.,* **24,** 2613–2616.

Chen, J., Inoue, T., Yurimoto, H. & Weidner, D.J., 2002. Effect of water on olivine-wadsleyite phase boundary in the $(Mg,Fe)_2SiO_4$ system, *Geophys. Res. Lett.,* **29,** 22-1–22-4.

Choy, G.L. & Richards, P.G., 1975. Pulse distortion and Hilbert transformation in multiply reflected and refracted body waves, *Bull. seism. Soc. Am.,* **65,** 55–70.

Cobden, L., Goes, S., Cammarano, F. & Connolly, J.A.D., 2008. Thermochemical interpretation of one-dimensional seismic reference models of the upper mantle: evidence for bias due to heterogeneity, *Geophys. J. Int.,* **175,** 627–648.

Connolly, J.A.D., 2005. Computation of phase equilibria by linear programming: a tool for geodynamic modeling and its application to subduction zone decarbonation, *Earth planet. Sci. Lett.,* **236,** 524–541.

Crotwell, H.P., Owens, T.J. & Ritsema, J., 1999. The TauP toolkit: flexible seismic travel-time and ray-path utilities, *Seismol. Res. Lett.,* **70,** 154–160.

Curtis, A. & Woodhouse, J.H., 1997. Crust and Upper mantle shear velocity structure beneath the Tibetan plateau and surrounding regions from interevent surface wave phase velocity inversion, *J. geophys. Res.-Solid Earth,* **102,** 11 789–11 813.

Davies, D., Kelly, E. & Filson, J., 1971. Vespa process for analysis of seismic signals, *Nat. Phys. Sci.,* **232,** 8–13.

Day, E.A. & Deuss, A., 2013. Reconciling *PP* and *P′P′* precursor observations of a complex 660 km discontinuity, *Geophys. J. Int.,* **194,** 834–838.

Deschamps, F., Cobden, L. & Tackley, P.J., 2012. The primitive nature of large low shear-velocity provinces, *Earth planet. Sci. Lett.*, **349–350,** 198–208.

Deuss, A., 2009. Global observations of mantle discontinuities using *SS* and *PP* precursors, *Surv. Geophys.,* **30,** 301–326.

Deuss, A. & Woodhouse, J.H., 2001. Seismic Observations of splitting of the mid-transition zone discontinuity in Earth's mantle, *Science,* **294,** 354–356.

Deuss, A. & Woodhouse, J.H., 2002. A systematic search for mantle discontinuities using *SS*-precursors, *Geophys. Res. Lett.,* **29,** doi:10.1029/2002GL014768.

Deuss, A., Redfern, S.A.T., Chambers, K. & Woodhouse, J.H., 2006. The nature of the 660-kilometer discontinuity in Earth's mantle from global seismic observations of *PP* precursors, *Science,* **311,** 198–201.

Dueker, K.G. & Sheehan, A.F., 1997. Mantle discontinuity structure from midpoint stacks of converted P to S waves across the Yellowstone hotspot track, *J. geophys. Res.-Solid Earth,* **102,** 8313–8327.

Duffy, T.S. & Anderson, D.L., 1989. Seismic velocities in mantle minerals and the mineralogy of the upper mantle, *J. geophys. Res.-Solid Earth,* **94,** 1895–1912.

Dziewonski, A.M. & Anderson, D.L., 1981. Preliminary reference Earth model, *Phys. Earth. planet. Inter.,* **25,** 297–356.

Efron, B. & Tibshirani, R., 1986. Bootstrap methods for standard errors, confidence intervals, and other measures of statistical accuracy, *Statistical Science,* **1,** 54–77.

Estabrook, C.H. & Kind, R., 1996. The nature of the 660-kilometer upper-mantle seismic discontinuity from precursors to the *PP* phase, *Science,* **264,** 1179–1182.

Fei, Y. *et al.*, 2004. Experimentally determined postspinel transformation boundary in Mg_2SiO_4 using MgO as an internal pressure standard and its geophysical implications, *J. geophys. Res.-Solid Earth,* **109,** B02305, doi:10.1029/2003JB002562.

Flanagan, M.P. & Shearer, P.M., 1998. Global mapping of topography on transition zone velocities by stacking *SS* precursors, *J. geophys. Res.-Solid Earth,* **103,** 2673–2692

Flanagan, M.P. & Shearer, P.M., 1999. A map of topography in the 410-km discontinuity from *PP* precursors, *Geophys. Res. Lett.,* **26,** 549–552.

Fuchs, K. & Müller, G., 1971. Computation of synthetic seismograms with the reflectivity method and comparison with observations, *Geophys. J. R. astr. Soc.,* **23,** 417–433.

Gasparik, T., 1996a, Diopside-jadeite join at 16–22 GPa, *Phys. Chem. Miner.,* **23,** 476–486.

Gasparik, T., 1996b, Melting experiments on the enstatite-diopside join at 70–224 kbar, including the melting of diopside, *Contrib. Miner. Petrol.,* **124,** 139–153.

Ghosh, S., Ohtani, E., Litasov, K.D., Suzuki, A., Dobson, D.P. & Funakoshi, K., 2013. Effect of water in depleted mantle on post-spinel transition and implication of 660 km seismic discontinuity, *Earth planet. Sci. Lett.,* **371–372,** 103–111.

Goldstein, P., Dodge, D., Firpo, M. & Minner, L., 2003. SAC2000: signal processing and analysis tools for seismologists and engineers, in *The IASPEI International Handbook of Earthquake and Engineering Seismology,* eds Lee, W.H.K., Kanamori, H., Jennings, P.C. & Kisslinger, C., Academic Press.

Gossler, J. & Kind, R., 1996. Seismic evidence for very deep roots of continents, *Earth planet. Sci. Lett.,* **138,** 1–13.

Grand, S.P. & Helmberger, D.V., 1984. Upper mantle shear structure of North America, *Geophys. J. Int.,* **76,** 399–438.

Grand, S.P., van der Hilst, R.D. & Widiyantoro, S., 1997. High resolution global tomography: a snapshot of convection in the Earth, *GSA Today,* **7,** 1–7.

Green, D.H., Hibbersen, W.O. & Jaques, A.L., 1979. Petrogenesis of mid-ocean ridge basalts, in *The Earth: Its Origin, Structure and Evolution,* pp. 269–299, ed. McElhinny, M.W., Academic Press.

Gu, Y., Dziewonski, A.M. & Agee, C.B., 1998. Global de-correlation of the topography of transition zone discontinuities, *Earth planet. Sci. Lett.,* **157,** 57–67.

Haines, S.S., Klemperer, S.L., Brown, L., Jingru, G., Mechie, J., Meissner, R., Ross, A. & Zhao Wenjin, Z., 2003. INDEPTH III seismic data: From surface observations to deep crustal processes in Tibet, *Tectonics,* **22,** doi:10.1029/2001TC001305.

Heit, B., Yuan, X., Bianchi, M., Kind, R. & Gossler, J., 2011. Study of the lithospheric and upper-mantle discontinuities beneath eastern Asia by *SS* precursors, *Geophys. J. Int.,* **183,** 252–266.

Helffrich, G.R., 2000. Topography of the transition zone seismic discontinuities, *Rev. Geophys.,* **38,** 141–158.

Helffrich, G.R. & Bina, C.R., 1994. Frequency dependence of the visibility and depths of mantle seismic discontinuities, *Geophys. Res. Lett.,* **21,** 2613–2616.

Hempel, S., Nissen-Meyer, T. & Thomas, C., 2013. The D′′ layer beneath the Northern Pacific, PICO presentation, in *Proceedings of the EGU General Assembly 2013,* Vienna, Austria.

Hill, R., 1965. Continuum micro-mechanics of elastoplastic polycrystals, *J. Mech. Phys. Solids,* **13,** 89–101.

Hirose, K., 2002. Phase transitions in pyrolitic mantle around 670-km depth: implications for upwelling of plumes form the lower mantle, *J. geophys. Res.-Solid Earth,* **107,** 2078, doi:10.1029/2001JB000597.

Hirose, K., Takafuji, N., Sata, N. & Ohishi, Y., 2005. Phase transition and density of subducted MORB crust in the lower mantle, *Earth planet. Sci. Lett.,* **237,** 239–251.

Hirschmann, M., 2006. Water, melting and the deep Earth H_2O cycle, *Ann. Rev. Earth planet. Sci.,* **34,** 629–653.

Hofmann, A.W., 1988. Chemical differentiation of the Earth—the relationship between mantle, continental crust and oceanic crust, *Earth planet. Sci. Lett.,* **90,** 297–314.

Houser, C., Masters, G., Flanagan, M. & Shearer, P., 2008. Determination and analysis of long-wavelength transition zone structure using *SS* precursors, *Geophys. J. Int.,* **174,** 178–194.

Irifune, T., 1987. An experimental investigation of the pyroxene-garnet transformation in a pyrolite composition and its bearing on the constitution of the mantle, *Phys. Earth planet. Inter.,* **45,** 324–336.

Irifune, T. *et al.* 1998. The postspinel phase boundary in Mg_2SiO_4 determined by in situ X-ray diffraction, *Science,* **279,** 1698–1700.

Irifune, T. & Ringwood, A.E., 1993. Phase transformations in subducted oceanic crust and buoyancy relationships at depths of 600–800 km in the mantle. *Earth planet. Sci. Lett.,* **117,** 101–110.

Ita, J. & Stixrude, L., 1992. Petrology, elasticity and composition of the mantle transition zone. *J. geophys. Res.-Solid Earth,* **97,** 6849–6866.

Jackson, I. & Rigden, S.M., 1998. Composition and temperature of the earth's mantle: seismological interpreted through experimental studies of earth materials, in *The Earth's Mantle: Composition, Structure and Evolution,* pp. 405–460, ed. Jackson, I., Cambridge University Press.

Jacobeit, E., Thomas, C. & Vernon, F., 2013. Influence of station topography and Moho depth on the mislocation vectors for the Kyrgyz Broadband Seismic Network (KNET), *Geophys. J. Int.,* **193,** 949–959.

Jacobsen, S.D., Smyth, J.R., Spetzler, H., Holl, C.M. & Frost, D.J., 2004. Sound velocities and elastic constants of iron-bearing hydrous ringwoodite, *Phys. Earth planet. Inter.,* **143–144,** 47–56.

Karato, S., 1997. On the separation of crustal component from subducted oceanic lithosphere near the 660 km discontinuity, *Phys. Earth planet. Inter.,* **99,** 103–111.

Katsura, T. *et al.* 2004. Olivine-wadsleyite transition in the system $(Mg,Fe)_2SiO_4$, *J. geophys. Res.-Solid Earth,* **109,** B02209, doi:10.1029/2003JB002438.

Kennett, B.L.N. & Engdahl, E.R., 1991. Traveltime for global earthquake location and phase identification, *Geophys. J. Int.,* **105,** 429–465.

Kennett, B.L. N., Engdahl, E.R. & Buhland, R., 1995. Constraints on seismic velocities in the Earth from travel-times, *Geophys. J. Int.,* **122,** 108–124.

Kind, R. *et al.* 2002. Seismic images of crust and upper mantle beneath Tibet: evidence for Eurasian Plate subduction, *Science,* **298,** 1219–1221.

King, D.W., Husebye, E.S. & Haddon, R.A.W., 1975. Precursors to *PP*, *Phys. Earth planet. Inter.,* **10,** 103–127.

King, D.W., Husebye, E.S. & Haddon, R.A.W., 1976. Processing of seismic precursor data, *Phys. Earth. planet. Inter.,* **12,** 128–134.

Kohlstedt, D.L., Keppler, H. & Rubie, D.C., 1996. Solubility of α, β and γ phases of $(Mg, Fe)_2SiO_4$, *Contrib. Miner. Petrol.,* **123,** 345–357.

Kosarev, G., Kind, R., Sobolev, S.V., Yuan, X., Hanka, W. & Oreshin, S., 1999. Seismic evidence for a detached Indian lithospheric mantle beneath Tibet, *Science,* **283,** 1306–1309.

Krüger, F. & Weber, M., 1992. The effect of low-velocity sediments on the mislocation vectors of the GRF array, *Geophys. J. Int.,* **108**(1) 387–393.

Lebedev, S. & van der Hilst, R.D., 2008. Global upper-mantle tomography with the automated multimode inversion of surface and S-waveforms, *Geophys. J. Int.,* **173,** 505–518.

Lee, C.-T.A. & Chen, W.P., 2007. Possible density segregation of subducted oceanic lithosphere along a weak serpentinite layer and implications for compositional stratification, *Earth planet. Sci. Lett.,* **255,** 357–366.

Li, C., van der Hilst, R., Meltzer, A.S. & Engdahl, E.R., 2008. Subduction of the Indian lithosphere beneath the Tibetan Plateau and Burma, *Earth planet. Sci. Lett.,* **274,** 157–168.

Li, L., Brodholt, J. & Alfè, D., 2009. Structure and elasticity of hydrous ringwoodite: a first principle investigation, *Phys. Earth planet. Inter.,* **177,** 103–115.

Litasov, K., 2010. The influence of Al_2O_3 on the H_2O content in periclase and ferropericlase at 25 GPa, Russ, *Geol. Geophys.,* **51,** 644–649.

Litasov, K., Ohtani, E., Langenhorst, F., Yurimoto, H., Kubo, T. & Kondo, T., 2003. Water solubility in Mg-perovskite, and water storage capacity in the lower mantle, *Earth planet. Sci. Lett.,* **211,** 189–203.

Litasov, K., Ohtani, E., Suzuki, A., Kawazoe, T. & Funakoshi, K., 2004. Absence of density crossover between basalt and peridotite in the cold slabs passing through 660 km discontinuity, *Geophys. Res. Lett.,* **31,** L24607, doi:10.1029/2004GL021306.

Litasov, K., Ohtani, E., Sano, A., Suzuki, A. & Funakoshi, K., 2005a, In situ X-ray diffraction study of post-spinel transformation in a peridotite mantle: implication for the 660-km discontinuity, *Earth planet. Sci. Lett.,* **238,** 311–328.

Litasov, K., Ohtani, E., Sano, A., Suzuki, A. & Funakoshi, K., 2005b, Wet subduction versus cold subduction, *Geophys. Res. Lett.,* **32,** doi:10.1029/2005GL022921.

Mao, Z., Jacobsen, S.D., Jiang, F., Smyth, J.R., Holl, C.M., Frost, D.J. & Duffy, T.S., 2008. Single crystal elasticity of wadsleyites, β-Mg_2SiO_4, containing 0.37–1.66 wt% H_2O, *Earth planet. Sci. Lett.,* **266,** 78–89.

Mao, Z., Jacobsen, S.D., Jiang, F., Smyth, J.R., Holl, C.M., Frost, D.J. & Duffy, T.S., 2010. Velocity crossover between hydrous and anhydrous forsterite at high pressures, *Earth planet. Sci. Lett.,* **293,** 250–258.

McDonough, W.F. & Sun, S.S., 1995. The composition of the Earth, *Chem. Geol,* **120,** 223–253.

Megnin, C. & Romanowicz, B, 2000. The three-dimensional shear velocity structure of the mantle from the inversion of body, surface and higher-mode waveforms, *Geophys. J. Int.,* **143,** 709–728.

Mendelssohn, M.J. & Price, G.D., 1997. Computer modelling of a pressure induced phase change in clinoenstatite pyroxenes, *Phys. Chem. Miner.,* **256,** 55–62.

Michael, P.J. & Bonatti, E., 1985. Peridotite composition from the North Atlantic: regional and tectonic variations and implications for partial melting, *Earth planet. Sci. Lett.,* **73,** 91–104.

Molnar, P. & Tapponnier, P., 1975. Cenozoic tectonics of Asia: effects of a continental collision, *Science,* **189,** 419–426.

Montagner, J.P. & Kennett, B.L.N., 1995. How to reconcile body-wave and normal-mode reference Earth models? *Geophys. J. Int.,* **125,** 229–248.

Muirhead, K. & Datt, R., 1976. N-th root process applied to seismic array data, *Geophys. J. R. astr. Soc.,* **47,** 197–210.

Müller, G., 1985. The reflectivity method: a tutorial, *J. Geophys.,* **58,** 153–174.

Nakanishi, I., 1986. Seismic reflections from the upper mantle discontinuities beneath the Mid-Atlantic Ridge observed by a seismic array in Hokkaido region, Japan, *Geophys. Res. Lett.,* **13,** 1458–1461.

Nakanishi, I., 1988. Reflections of *P′P′* from upper mantle discontinuities beneath the Mid-Atlantic Ridge, *Geophys. J.,* **93,** 335–346.

Neele, F. & Snieder, R., 1992. Topography of the 400 km discontinuity from observation of long-period P400P phases, *Geophys. J. Int.,* **109,** 670–682.

Neele, F., de Regt, H. & VanDecar, J., 1997. Gross errors in upper mantle discontinuity topography from underside reflection data, *Geophys. J. Int.,* **129,** 194–204.

Ohtani, E., Mizobata, H. & Yurimoto, H., 2000. Stability of dense hydrous magnesium silicate phases in the system Mg_2SiO_4-H_2O and $MgSiO_3$-H_2O at pressures up to 27 GPa, *Phys. Chem. Miner,* **27,** 533–544.

Ono, S., Ito, E. & Katsura, T., 2001. Mineralogy of subducted basaltic crust (MORB) from 25 to 37 GPa, and chemical heterogeneity of the lower mantle, *Earth planet. Sci. Lett.,* **190,** 57–63.

Ono, S., Ohishi, Y., Isshiki, M. & Watanuki, T., 2005. In situ X-ray observations of phase assemblages in peridotite and basalt compositions at lower mantle conditions: Implications for density of subducted oceanic plate, *J. geophys. Res.-Solid Earth,* **110,** B02208, doi:10.1029/2004JB003196.

Perrillat, J.P., Ricolleau, A., Daniel, I., Fiquet, G., Mezouar, M., Guignot, N. & Cardon, H., 2006. Phase transformations of subducted basaltic crust in the upmost lower mantle, *Phys. Earth planet. Inter.,* **157,** 139–149.

Poli, S. & Schmidt, M.W., 2002. Petrology of subducted slabs, *Ann. Rev. Earth Planet. Sci.,* **30,** 207–235.

Ranero, C.R., Phipps-Morgan, J., McIntosh, K. & Reichert, C., 2003. Bending-related faulting and mantle serpentinization at the Middle America trench, *Nature,* **425,** 367–373.

Rawlinson, N. & Kennett, B.L. N., 2004. Rapid estimation of relative and absolute delay time across a network by adaptive stacking, *Geophys. J. Int.,* **157,** 332–340.

Reuss, A., 1929. Berechnung der Fließgrenze von Mischkristallen auf Grund der Konstanten des Einkristalls, *Z. Angew. Math. Mech.,* **9,** 49–58.

Revenaugh, J. & Jordan, T., 1991. Mantle layering from ScS reverberations: 3. the upper mantle, *J. geophys. Res.-Solid Earth,* **96,** 19 781–19 810.

Revenaugh, J. & Sipkin, S.A., 1994. Seismic evidence for silicate melt atop the 410-km mantle discontinuity, *Nature,* **369,** 474–476.

Ricolleau, A. *et al.* 2010. Phase relations and equation of state of a natural MORB: implications for the density profile of subducted oceanic crust in the Earth's lower mantle, *J. geophys. Res.-Solid Earth,* **115,** B08202, doi:10.1029/2009JB006503.

Ringwood, A.E., 1967. The pyroxene-garnet transformation in the Earth's mantle, *Earth planet. Sci. Lett.,* **2,** 255–263.

Ringwood, A.E., 1969. Phase transformations in the Mantle, *Earth planet. Sci. Lett.,* **5,** 401–412.

Ringwood, A.E., 1979. *Origin of the Earth and Moon,* Springer-Verlag.

Ringwood, A.E. & Irifune, T., 1988. Nature of the 650-km seismic discontinuity: implications for mantle dynamics and differentiation, *Nature,* **331,** 131–136.

Ritsema, J., Deuss, A., van Heijst, H.J. & Woodhouse, J.H., 2011. S40RTS: a degree-40 shear-velocity model for the mantle from new Rayleigh wave dispersion, teleseismic travel time and normal-mode splitting function measurements, *Geophys. J. Int.,* **184**(3), 1223–1236.

Rost, S. & Thomas, C., 2002. Array seismology: methods and applications, *Rev. Geophys.,* **40,** 2-1–2-27.

Rost, S. & Thomas, C., 2009. Improving seismic resolution through array processing techniques, *Surv. Geophys.,* **30,** 271–299.

Rost, S. & Weber, M., 2002. The upper mantle transition zone discontinuities in the Pacific as determined by short-period data, *Earth planet. Sci. Lett.,* **204,** 347–361.

Rost, S., Garnero, E.J. & Williams, Q., 2008. Seismic Array Detection of subducted oceanic crust in the lower mantle, *J. geophys. Res.-Solid Earth,* **113,** B06303, doi:10.1029/2007JB005263.

Ryberg, T., Wenzel, F., Egorkin, A.V. & Solodilov, L., 1998. Properties of the mantle transition zone in northern Eurasia, *J. geophys. Res.-Solid Earth,* **103,** 811–822.

Sanchez-Valle, C., Sinogeikin, S., Smyth, J. & Bass, J.D., 2006. Single-crystal elastic properties of dense hydrous magnesium silicate phase A, *Am. Mineral.,* **91,** 961–971.

Sanchez-Valle, C., Sinogeikin, S., Smyth, J. & Bass, J.D., 2008. Sound velocities and elasticity of DHMS phase A to high pressure and implications for seismic velocities and anisotropy in subducted slabs, *Phys. Earth planet. Inter.,* **170,** 229–239.

Saikia, A., Frost, D.J. & Rubie, D.C., 2008. Splitting of the 520-kilometer seismic discontinuity and chemical heterogeneity in the mantle, *Science,* **319,** 1515–1518.

Schmerr, N. & Garnero, E.J., 2006. Investigation of upper mantle discontinuity structure beneath the central Pacific using *SS* precursors, *J. geophys. Res.-Solid Earth,* **111,** B08305, doi:10.1029/2005JB004197.

Schmerr, N. & Garnero, E.J., 2007. Upper mantle discontinuity topography from thermal and chemical heterogeneity, *Science,* **318,** 623–626.

Schmerr, N. & Thomas, C., 2011. Subducted lithosphere beneath the Kuriles from migration of *PP* precursors, *Earth planet. Sci. Lett.,* **311,** 101–111.

Shearer, P.M., 1990. Seismic imaging of upper mantle structure with new evidence for a 520 km discontinuity, *Nature,* **344,** 121–126.

Shearer, P.M., 1991. Constraints on upper mantle discontinuities from observations of long-period reflected and converted phases, *J. geophys. Res.-Solid Earth,* **96,** 18 147–18 182.

Shearer, P.M., 2000. Upper mantle in discontinuities, in *Earth's Deep Interior: Mineral Physics and Tomography from the Atomic to the Global Scale,* pp. 115–131, eds Karato, S., Forte, A.M., Liebermann, R.C., Masters, G. & Stixrude, L., AGU.

Shearer, P.M. & Flanagan, M.P., 1999. Seismic velocity and density jumps across the 410- and 660-kilometer discontinuities, *Science,* **285,** 1545–1548.

Shearer, P.M. & Masters, T.G., 1992. Global mapping of topography on the 660 km discontinuity, *Nature,* **355,** 791–796.

Shim, S.H., Duffy, T.S. & Shen, G., 2001. The post-spinel transformation in Mg_2SiO_4 and its relation to the 660-km seismic discontinuity, *Nature,* **411,** 571–574.

Simmons, N. & Gurrola, H., 2000. Multiple seismic discontinuities near the base of the transition zone in the mantle, *Nature,* **405,** 559–562.

Sleep, N.H., 1990. Hotspots and mantle plumes: some phenomenology, *J. geophys. Res.-Solid Earth,* **95,** 6715–6736.

Smyth, J.R. & Frost, D.J., 2002. The effect of water on the 410-km discontinuity: an experimental study, *Geophys. Res. Lett.,* **29,** 1485–1489.

Song, T.R. A., Helmberger, D.V. & Grand, S., 2004. Low velocity zone atop the 410 km seismic discontinuity in the northwestern United States, *Nature,* **427,** 530–533.

Stammler, K., 1993. Seismic Handler: programmable multichannel data handler for interactive and automaticprocessing of seismological analysis, *Comput. Geosci.,* **19,** 135–140.

Stern, R.J., 2000. Subduction zones, *Rev. Geophys.,* **40,** 3-1–3-37.

Stixrude, L., 1997. Structure and sharpness of phase transitions and mantle discontinuities, *J. geophys. Res.-Solid Earth,* **102,** 14 835–14 852.

Stixrude, L. & Lithgow-Bertelloni, C., 2005. Thermodynamics of mantle minerals–I. Physical properties, *Geophys. J. Int.,* **162,** 610–632.

Stixrude, L. & Lithgow-Bertelloni, C., 2011. Thermodynamics of mantle minerals – II. Phase equilibria, *Geophys. J. Int.,* **184,** 1180–1213.

Sun, S.S., 1982. Chemical-composition and origin of the earth's primitive mantle, *Geochim. Cosmochim. Acta,* **46,** 179–192.

Suzuki, A., Ohtani, E., Morishima, H., Kubo, T., Kanbe, Y. & Kondo, T., 2000. In situ determination of the phase boundary between wadsleyite and ringwoodite in Mg_2SiO_4, *Geophys. Res. Lett.,* **27,** 803–806.

Tapponnier, P., Zhiqin, X., Roger, F., Meyer, B., Arnaud, N., Wittlinger, G. & Jingsui, Y., 2001. Oblique Stepwise Rise and Growth of the Tibet Plateau, *Science,* **294,** 1671–1677.

Thomas, C. & Billen, M., 2009. Upper mantle structure along a profile in the southwest Pacific, *Geophys. J. Int.,* **176,** 113–125.

Tilmann, F. & Ni, J. INDEPTH III Seismic Team, 2003. Seismic imaging of the downwelling Indian lithosphere beneath Central Tibet, *Science,* **300,** 1424–1427.

Trampert, J., Deschamps, F., Resovsky, J. & Yuen, D., 2004. Probabilistic tomography maps chemical heterogeneities throughout the lower mantle, *Science,* **306,** 853–856.

Vacher, P., Mocquet, A. & Sotin, C., 1998. Computation of seismic profiles from mineral physics: the importance of the non-olivine components for explaining the 660 km depth discontinuity, *Phys. Earth planet. Inter.,* **106,** 275–298.

van der Voo, R., Spakman, W. & Bijwaard, H., 1999. Tethyan slabs under India, *Earth planet. Sci. Lett.,* **171**(1), 7–20.

Vinnik, L., 1977. Detection of waves converted from P to SV in the mantle, *Phys. Earth planet. Inter.,* **15,** 39–45.
Voigt, W., 1928. *Lehrbuch der Kristallphysik,* Teubner.
Wang, J., Sinogeikin, S.V., Inoue, T. & Bass, J.D., 2003. Elastic properties of hydrous ringwoodite, *Am. Mineral.,* **88,** 1608–1611.
Wang, Y., Uchida, T., Zhang, J., Rivers, M.L. & Sutton, S.R., 2004. Thermal equation of state of akimotoite $MgSiO_3$ and effects of the akimotoite-garnet transformation on seismic structure near the 660 km discontinuity, *Phys. Earth planet. Inter.,* **143/144,** 57–80.
Weidner, D.J., 1985. A mineral physics test of a pyrolite mantle, *Geophys. Res. Lett.,* **12,** 417–420.
Weidner, D.J. & Wang, Y., 1998. Chemical and Clapeyron-induced buoyancy at the 660-km discontinuity, *J. geophys. Res.-Solid Earth,* **103,** 7431–7441.
Weidner, D.J. & Wang, Y., 2000. Phase transformations: implications for mantle structure, *AGU Monography, Mineral Physics and Tomography from the Atomic to the Global Scale Geophysical Monograph,* **117,** 215–235.
Wessel, P. & Smith, W.H. F., 1995. New version of the Generic Mapping Tools released, *EOS, Trans. Am. geophys. Un.*, **76,** 329.
Willet, S.D. & Beaumont, C., 1994. Subduction of Asian lithopsheric mantle beneath Tibet inferred from models of continental collision, *Nature,* **369,** 643–645.
Williams, Q. & Revenaugh, J., 2005. Ancient subduction, mantle eclogite, and the 300 km seismic discontinuity, *Geology,* **33,** 1–4.
Woodland, A.B. & Angel, R.J., 1997. Reversal of the orthoferrosilite-high-p clinoferrosilite transition, a phase diagram for $FeSiO_3$ and implications for the mineralogy of the earth's upper mantle, *Eur. J. Mineral.,* **9,** 245–254.
Workman, R.K. & Hart, S.R., 2005. Major and trace element composition of the depleted MORB mantle (DMM), *Earth planet. Sci. Lett.* **231,** 53–72.
Xu, F., Vidale, J., Earle, P. & Benz, H., 1998. Mantle discontinuities under southern Africa from precursors to $P'P'$df, *Geophys. Res. Lett.,* **25,** 571–574.
Yin, A. & Harrison, T.M., 2000. Geologic evolution of the Himalayan-Tibetan orogen, *Ann. Rev. Earth planet. Sci.,* **28,** 211–280.
Zhao, W. *et al.*, 2011. Tibetan plate overriding the Asian plate in central and northern Tibet, *Nature Geosci.,* **4,** 870–873.
Zheng, Z. & Romanowicz, B., 2012. Do double '*SS* precursors' mean double discontinuities? *Geophys. J. Int.,* **191,** 1361–1373.

SUPPORTING INFORMATION

Additional Supporting Information may be found in the online version of this article:

Figure S1. Thermodynamic modelling with Perple_X. (a) Scheme of thermodynamic modelling and forward modelling of seismic properties with Perple_X (Connolly 2005) using the database of elastic properties and the solid solution model of Stixrude & Lithgow-Bertelloni (2011). (b) *T*-*z* profiles for adiabats with potential temperatures between 800 and 1500 °C (calculated after Cobden *et al.* 2008). The red adiabat indicates the 1300 °C potential temperature adiabat and is denoted as the average mantle geotherm.

Figure S2. Profiles of seismic properties for harzburgite, pyrolite, piclogite and MORB mantle compositions along the adiabats of figure S1b around 520 km depth, calculated with Perple_X. (a) *P*-wave velocity. (b) *S*-wave velocity. (c) Density.

Figure S3. Transition pressure and depth of mineral transformations for possible bulk mantle compositions around 410, 520 and 660 km depth. The error bars indicate a pressure uncertainty of 0.6 GPa (Smyth & Frost 2002). The Clapeyron slopes of the mineral transformations are fit as the linear regression of the transition pressures. (a) Mineral transformations around 410 km depth. ol: olivine, wad: wadsleyite. (b) Mineral transformations around 520 km depth. wad: wadsleyite, rg: ringwoodite, cpx: clinopyroxene, capv: calcium perovskite. (c) Mineral transformations around 660 km depth for pyrolite mantle composition. rg: ringwoodite, gt: garnet, il: ilmenite, mw: magnesiowuestite, pv: perovskite. (d) Same as (c), but for piclogite mantle composition. (e) Same as (c), but for harzburgite mantle composition. (f) Same as (c), but for MORB mantle composition.

Figure S4. Profiles of seismic properties for harzburgite, pyrolite, piclogite and MORB mantle compositions along the adiabats of figure S1b around 660 km depth, calculated with Perple_X. (a) *P*-wave velocity. (b) *S*-wave velocity. (c) Density.

Table S1. Data Sources, total number of array data sets used for investigating *PP* and *SS* underside reflections, number of data sets with visible *PP* or *SS* waveforms and number of array data sets with underside reflections. No events are used when the last column is marked with a –.

Table S2. Event locations of earthquakes showing *PP* and *SS* underside reflections off mantle transition zone discontinuities. Earthquake parameters are from the Preliminary Determination of Earthquakes (PDE) catalogue of the NEIC. Events with a – for all reflectors show no underside reflections despite good data quality. Reflectors in the columns denoted with 'dX' refer to reflectors apart from the reflections off the 410 or the 660 km discontinuity. For network abbreviations use Table S1.

Table S3. Bulk chemical compositions used for the computation of phase equilibria with Perple_X.

Table S4. Overview on the range of bulk chemical compositions of pyrolite, piclogite, harzburgite and MORB. Compositions marked with ∗ denote bulk chemical compositions given in weight percentages.

Table S5. Clapeyron slopes of mineral transformations as derived for the used compositions in Table S3 by the Perple_X calculations of this study (http://gji.oxfordjournals.org/lookup/suppl/doi:10.1093/gji/ggt511/-/DC1).

Please note: Oxford University Press is not responsible for the content or functionality of any supporting materials supplied by the authors. Any queries (other than missing material) should be directed to the corresponding author for the article.